Pedro de Abreu Avó Baião

Licenciado em Ciências de Engenharia de Materiais

Nanostructuring silicon probes via electrodeposition: Characterization of electrode coatings for acute *in vivo* neural recordings

Dissertação para obtenção do Grau de Mestre em
Engenharia de Micro e Nanotecnologias

Orientador: Adam Kampff, Professor Doutor,
Champalimaud Center for the Unknown

Co-orientador: Elvira Fortunato, Professora Doutora,
Faculdade de Ciências e Tecnologia da Universidade Nova de Lisboa

Júri:

Presidente: Prof. Doutor Rodrigo Ferrão Paiva Martins
Arguente: Prof. Doutor Rui Alberto Garção Barreira do Nascimento Igreja
Vogal: Prof. Doutor Adam Raymond Kampff

FACULDADE DE
CIÊNCIAS E TECNOLOGIA
UNIVERSIDADE NOVA DE LISBOA

Novembro, 2014

NANOSTRUCTURING SILICON PROBES VIA ELECTRODEPOSITION: CHARACTERIZATION OF ELECTRODE COATINGS FOR ACUTE *IN VIVO* NEURAL RECORDINGS

Faculdade de Ciências e Tecnologia
Universidade Nova de Lisboa

So the future is like a huge freight train barreling down the tracks, headed our way. Behind this train is the sweat and toil of thousands of scientists who are inventing the future in their labs. You can hear the whistle of the train. It says: biotechnology, artificial intelligence, nanotechnology, and telecommunications. However, the reaction of some is to say, "I am too old. I can't learn this stuff. I will just lie down and get run over by the train." However, the reaction of the young, the energetic, and the ambitious is to say, "Get me on that train! This train represents my future. It is my destiny. Get me in the driver's seat."

Michio Kaku

Acknowledgements

I would like to thank everyone who have made this dissertation possible. It has been a trying and interesting time in my life. I know and I'm truly sorry for not mentioning everyone that fully supported me on this project and throughout my bachelors and master's degree. But with that said, I dearly hope I'm able to make justice to everyone by honoring and paying tribute to them here. I would like to highlight and sincerely thank the following:

To Dr. Adam Kampff for giving me the chance to work alongside an amazing team at the Champalimaud Center of the Unknown (CCU) and an experience that will not be forgotten. It truly was an amazing opportunity to elaborate on such an interesting and daring topic with the possibility to contribute on improving further knowledge in this research field. I would also like to express my gratitude for the useful comments, remarks and engagement through the learning process of this master thesis.

To Prof. Elvira Fortunato from the moment I attended her Microelectronic I lectures till the moment was given complete trust to extend my work beyond CENIMAT/I3N. Also, being allowed work in her research group having full support and guidance. Along with Prof. Rodrigo Martins, and by putting a tremendous effort, expertise and passion for science, they built fully equipped laboratories and established crucial relations with national and international partners, creating the scientific and financial basis that allowed this and many other research works to be developed.

To Joana Neto for allowing me to work alongside her and continue to explore her work. The tremendous patience for inserting me in a topic I was completely oblivious and guiding me every day from the start till the end of my dissertation. Without her this project wouldn't have been possible and I'm truly grateful for what she thought me and for the enormous help tackling many of the scientific and practical hurdles we've encountered along the way.

To Kinga Kocsis for being so helpful and having such an enormous patience in analyzing surgery recordings and introducing spike sorting methods. Data analysis would have been so much easier if you had been in Portugal helping us from the start of this project. Thank you so much for the tremendous help you've offered and provided.

I would also like to thank the rest of the members of the Intelligent Systems Lab at the CCU who I was proud to work alongside and discuss many topics with: George Dimitriadis, Gonçalo Lopes, Joana Nogueira, João Frazão and Pedro Lacerda.

To Prof. Pedro Barquinha and Dra. Daniela Gomes for the long hours spent at the scanning electron microscope where hundreds of images were taken, combined with the constant panic of damaging or breaking silicon probes.

To Lídia Santos for her insights on tungsten oxide synthesis and always being ready to help when needed. Together with Dra. Rita Branquinho, I was able to fully comprehend the electrochemical phenomena occurring on this project.

To everyone at CENIMAT/I3N that provided me a great work environment and an amazing experience.

To my colleagues and friends who I've met at Faculdade de Ciências e Tecnologia (FCT) and who've accompanied me from the start of my bachelor's in Materials Science until the end of my master's in Micro and Nanotechnology: Alexandre Oliveira, Ana Catarina, Ana Kullberg, Ana Paula, Ana Rita, Daniel Matos, Gonçalo Rodrigues, Joana Fernandes Miguel Soares, Paul Grey, Pedro Loures, Ricardo Marreiros, Rita Pontes, Rute Almedia and Vasco Rodrigues. Also to my long date friends who've accompanied from my early stages till this moment: André Pontes and Luis Marques. Thanks for all the moments filled with stupidity and joy.

I would like to thank my loved ones, starting with my family, who have supported me throughout the entire process. To my mom and grandmother for putting up with me for the past 24 years and for making me the man I am today. A moment I truly want to dedicate to them. To my father, his wife and my siblings for their understanding in my absence in their lives and for the strength they gave me throughout the years.

To my girlfriend and longtime best friend, Tânia Marques, for keeping me harmonious, happy, peaceful and sane. Without you I would be lost and I will be forever grateful for your love.

Resumo

Para compreender o funcionamento do cérebro são necessárias ferramentas capazes de medir a atividade elétrica de neurónios a uma grande escala. Todavia, são necessários progressos para aumentar o número de neurónios registados e identificados simultaneamente com microeléctrodos existentes. Este projeto tem como objetivo avaliar como diferentes materiais podem modificar a eficiência da transferência de sinal entre o tecido neuronal e elétrodos.

Dessa forma, diversos materiais para revestimento (ouro, PEDOT, óxido de tungsténio, nanotubos de carbono) foram caracterizados em termos dos fenómenos eletroquímicos e eficiência de aquisição de sinal. Elétrodos de irídio (177-706 μm^2) foram revestidos através de deposições galvanostáticas sob diferentes densidades de carga.

Através de espectroscopia de impedância (EIS) em solução salina foi determinado que o módulo da impedância a 1 kHz depende do material de revestimento e diminui um máximo de duas ordens de magnitude para PEDOT (1 MΩ para 25 kΩ). Os elétrodos foram também caracterizados por voltametria cíclica (CV) demonstrando um aumento de uma ordem de magnitude na capacidade de armazenamento de carga, alcançando um máximo de 84.1 mC/cm^2 para o compósito PEDOT:nanopartículas de ouro (aumento de 38 vezes na capacidade).

Gravação da atividade neuronal espontânea no córtex foi efetuada em roedores anestesiados para avaliar o desempenho dos revestimentos de elétrodos.

Palavras-chave: neurónios, microeléctrodos, electrodeposição, impedância, voltametria cíclica, potencial de acção.

Abstract

Understanding how the brain works will require tools capable of measuring neuron electrical activity at a network scale. However, considerable progress is still necessary to reliably increase the number of neurons that are recorded and identified simultaneously with existing microelectrode arrays. This project aims to evaluate how different materials can modify the efficiency of signal transfer from the neural tissue to the electrode.

Therefore, various coating materials (gold, PEDOT, tungsten oxide and carbon nanotubes) are characterized in terms of their underlying electrochemical processes and recording efficacy. Iridium electrodes (177-706 μm^2) are coated using galvanostatic deposition under different charge densities.

By performing electrochemical impedance spectroscopy in phosphate buffered saline it is determined that the impedance modulus at 1 kHz depends on the coating material and decreased up to a maximum of two orders of magnitude for PEDOT (from 1 MΩ to 25 kΩ). The electrodes are furthermore characterized by cyclic voltammetry showing that charge storage capacity is improved by one order of magnitude reaching a maximum of 84.1 mC/cm^2 for the PEDOT: gold nanoparticles composite (38 times the capacity of the pristine).

Neural recording of spontaneous activity within the cortex was performed in anesthetized rodents to evaluate electrode coating performance.

Keywords: neurons, microelectrodes, electrodeposition, impedance, cyclic voltammetry, action potential.

Symbols

A	Area of the electrodes (μm^2)
$\mathbf{C_H}$	Helmholtz capacitance (F)
CPE1	Constant phase element 1 ($S.s^{1/2}$)
CPE2	Constant phase element 2 ($S.s^{1/2}$)
CPE3	Constant phase element 3 ($S.s^{1/2}$)
$\mathbf{C_{sc}}$	Charge storage capacity (mC/cm^2)
$\mathbf{D_{OHP}}$	Distance to the Outer Helmholtz Plane
$\boldsymbol{\varepsilon_0}$	Vacuum permittivity (F/m)
$\boldsymbol{\varepsilon_r}$	Relative static permittivity (a.u)
n	Phase of the CPE
$\mathbf{P2P_{avg}}$	Peak to Peak average amplitude value (µV)
$\mathbf{R_E}$	Resistance of the electrolyte seen by the electrode (Ω)
$\mathbf{R_p}$	Resistance of the porous structure (Ω)
$\mathbf{R_{CT1}}$	Charge transfer resistance 1 (Ω)
$\mathbf{R_{CT2}}$	Charge transfer resistance 2 (Ω)
SNR	Signal to noise ratio (a.u)
STDV	Standard deviation (µV)
$\mathbf{Y_0}$	Adjustable parameter containing the diffusion coefficient ($S.s^{1/2}$)
$\mathbf{Y_{0CPE1}}$	Adjustable parameter containing the diffusion coefficient 1 ($S.s^{1/2}$)
$\mathbf{Y_{0CPE2}}$	Adjustable parameter containing the diffusion coefficient 2 ($S.s^{1/2}$)
$\mathbf{Y_{0CPE3}}$	Adjustable parameter containing the diffusion coefficient 3 ($S.s^{1/2}$)
$\boldsymbol{\omega}$	Angular frequency (rad/s)
W	Warburg diffusion element ($S.s^{1/2}$)
Z	Impedance (Ω)
$\mathbf{Z_{ac}}$	Impedance value after coating (Ω)
$\mathbf{Z_{drop}}$	Impedance drop from the initial value to post-coating value (a.u)
$\mathbf{Z_i}$	Impedance value before coating (Ω)
$\mathbf{Z_T}$	Total impedance of the equivalent circuit (Ω)

Abbreviations

Au	Gold
ALS	Amyotrophic Lateral Sclerosis
Au NPs	Gold Nanoparticles
C	Carbon
Cl	Chlorine
CNT	Carbon Nanotubes
CV	Cyclic Voltammetry
DLS	Dynamic Light Scattering
ECM	Extracellular membrane
EEG	Electroencephalography
EF	Extracellular Fluid
EDL	Electrochemical Double Layer
EIS	Electrochemical Impedance Spectroscopy
ECEI	Electrode-Coating-Electrolyte Interface
fMRI	functional Magnetic Resonance Imaging
FETs	Field Effect Transistors
HDP	High Density Probe
MEMS	Microelectromechanical Systems
MW	Multi-Wall
Na	Sodium
O	Oxygen
PEDOT	Poly(3,4-ethylenedioxythiophene)
PET	Positron Emission Tomography
P2P	Peak-To-Peak Amplitude
PSS	Poly(styrenesulfonate)
PVP	Polyvinylpyrrolidone
R.E	Reference Electrode
S	Sulphur

SDS	Sodium Dodecyl Sulfate
SEM	Scanning Electron Microscopy
Si	Silicon
W	Tungsten
XRD	X-Ray Diffraction
WO_3	Tungsten Oxide
WO_3 NPs	Tungsten Oxide Nanoparticles
W.E	Working Electrode

Table of Contents

Figure Index

Table Index

1. Introduction

1.1. Overview

Steady progress in biology and medicine has led to major advances in our comprehension of how complex living systems function. However, one of the ultimate challenges facing science and engineering remains – understanding how the brain works. Developing a theory explaining brain functionality would not only be a major advance in the field of biology, but it would also open paths allowing the comprehension of the pathophysiology of neurological and neuropsychiatric diseases such as Alzheimer's, Parkinson's, Amyotrophic Lateral Sclerosis (ALS), Dementia and Epilepsy. [1] But even with the enormous efforts and substantial progress made by neuroscientists trying to comprehend the molecular and cellular components of neural circuits both in humans and in animals, an all-encompassing theory explaining how the brain works is yet to be found. [2]

Hence, continued progress in neuroscience is vital yet with approximately eighty-five billion neurons, one hundred trillion synapses and over one hundred chemical neurotransmitters in the human brain, this is an overwhelming task. Communication between neurons is the cellular basis for thinking, decision making and control of muscular movement. [3]

Neurons are specialized cells that input, process, store and output information through electrical and chemical signals in four basic paths: (i) Ca^{2+} evoked exocytosis with chemical neurotransmission, (ii) gap junction electronic coupling, (iii) secretion of neurosteroids, nitric oxide and derivatives of the arachidonic acid acting in paracrine manner, and (iv) cellular adhesive protein interaction with scaffold protein reorganization. [4] At rest, the neuron's cell membrane has an excess of positive charges at the extracellular surface, and the cytoplasm an excess of negative charge. The charge separation gives rise to a voltage across the membrane called membrane potential [5]. Temporary changes in the current flow into and out of the cell produce electrical signals that drive a potential across the cell membrane – action potential (Figure 1.1). These produce a large transmembrane voltage change due to the ionic movement across the membrane through voltage-gated channels in the vicinity of the soma (axon hillock) that can be detected in the extracellular environment by placing a conductor in close proximity to the neuron. The electrodes record a combined extracellular signal gathered from all the spiking neurons in its vicinity and the contribution of a single neuron depends on its distance to the electrode. [6, 7]

Developments in the recording and stimulation of neuronal activity has had many applications in different areas of biomedicine such as neural interface systems, systems to assist in the understanding of neural network behavior, drug discovery pharmacology and cell-based biosensors. [8] In one hand, the use of non-invasive tools allows whole brain imaging through different available techniques (electroencephalography (EEG), positron emission tomography (PET) and functional magnetic resonance imaging (fMRI)) that span the scale of both spatial and temporal resolution. [9] On the other hand, by using invasive techniques it’s possible to visualize populations and networks of neurons. [10,11,12]

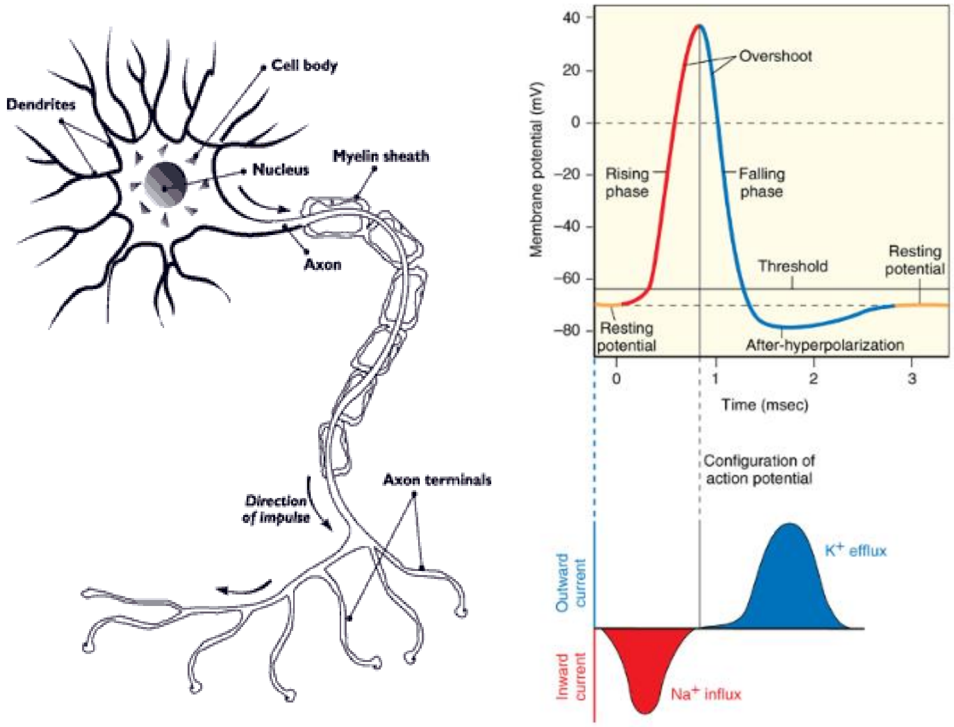

Figure 1.1 – The structure of a neuron. Axons are the transmitting element of neurons: Most axons in the central nervous system are very thin (between 0.2 and 20 µm in diameter) compared with the cell body (50 µm or more). The axon terminals of the presynaptic neuron transmit signals to the postsynaptic cells (a). Configuration of an action potential: (b) phases of an action potential and (c) inward and outward current of Na$^+$ and K$^+$. [13]

Therefore, the use of invasive tools to record the electrical brain activity has led to significant advances in basic neuroscience. [14] In the past, neuroscience research focused on the recording of single neurons due to their available tools (single wires for example). However, the need of retrieving information from complex neuron networks has led to the creation of new systems such as arrays of wires, silicon shafts and other complex micro machined silicon systems; all of these with a capability for probing simultaneously more individual neurons. [15]

Technologies have evolved from early electrolyte-filled micropipettes to the current emerging microelectromechanical systems (MEMS) and polymer electrodes (flexible electrodes), to more specific hybrid neuronal probes which have the combined capability to record electrical activity, specific neural biochemical markers and even stimulate and silence neurons optically. [16, 17, 18]

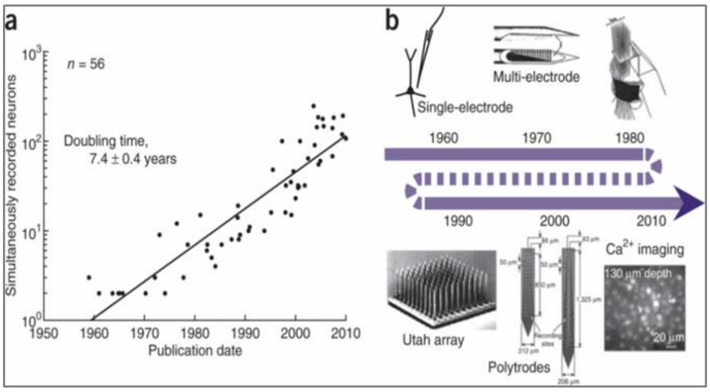

Figure 1.2 – Exponential growth in the number of recorded neurons seen on (a). The number of simultaneously recorded neurons doubled approximately every 7 years; (b) shows a timeline of recording technology development from single-electrode recordings to multi-electrode arrays and *in vivo* imaging techniques. [19]

As shown in Figure 1.2, the development from single-electrode recordings to multi-electrode arrays and *in vivo* imaging techniques has increased the number of simultaneously recorded neurons. Optical imaging of multiple single neurons is a recent promising development in this field. However, this approach is too slow to monitor action potentials and is not practical for monitoring deep cortical activity. [20] To achieve high spatial resolution of neural recording with extracellular probes, efforts are underway to produce ultra-high density probes with small electrodes (< 10 μm) arranged in dense arrays. [21] Micro and nanosystems technology allow for the arrangement of multiple microelectrodes on the same substrate over small distances. Thus, there is a possibility for simultaneous recording from many neurons. However, to accomplish this task, and in order to optimize the recorded data and allow identification of all adjacent neurons, a high quality signal from the nearby tissue must be obtained. [22, 23] With current electrodes, there are problems and fundamental limits for the current materials used in respect to charge storage capacity and impedance. Therefore, it is desired to develop microelectrodes for simultaneous monitoring of neural activity from multiple neurons in order to record *in vivo* neural activity from the largest number of neurons possible distributed in different places throughout the brain. [24] Improving existing tools, as proposed in this thesis, promotes a connection between neuroscience and nanotechnology and allow both the possibility of mapping neuronal circuits and to comprehend brain functionality. [25]

1.2. Electrode-tissue interface

The two principles behind the transduction of electrical signals from the ionic world of the neural tissue to the microelectrodes have been reported extensively in the literature as a capacitive coupling and charge transfer mechanism. [26] The chemical and electrochemical reactions that take place at the surface of the microelectrodes when exposed to the extracellular fluid (EF) of the neural tissue generate a space-charge region on the fluid also known as electrochemical double layer (EDL) The ionic currents from activated neurons can transiently modify this charge distribution and induce changes on the interfacial potential that can be easily detected. [27]

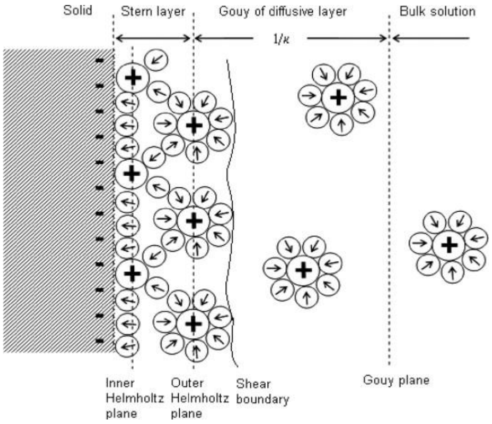

Figure 1.3 – Gouy-Chapman-Stern model of the Electrochemical Double Layer (EDL). [27]

The exact nature of this charge distribution depends on the conductor material, the surface properties of the microelectrode, as well as on the amplitude and frequency of the electrical signals involved, and is the key for understanding the signal transduction across the electrode-tissue interface. [22]

1.3. Electrode modifications

For recording electrodes, different materials have been used such as platinum, gold, tungsten, iridium and even stainless steel taking usually in consideration the impedance magnitude at 1 kHz (biological relevant frequency of a neural action potential). [28, 29]

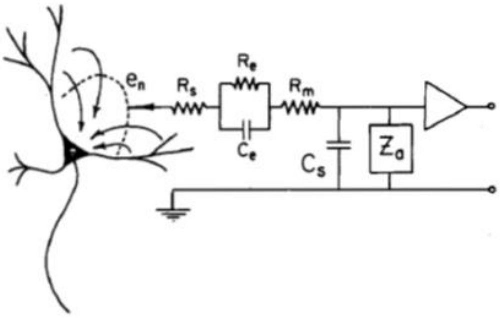

Figure 1.4 – Equivalent circuit of a metal microelectrode recording from the isopotential line ‘en’ of a neuron in a conductor volume. [30]

Metal electrode-tissue interface can be represented by a parallel R_eC_e combination in series with the resistances, R_m and R_S, due to the metal interconnects and the solution, respectively. The frequency-dependent impedance Z (jω), where j is the imaginary number and ω is the angular frequency.

$$Z\,(j\omega) = Z' + jZ'' = R_s + \frac{R_e}{1+(\omega R_e C_e)^2} - j\frac{\omega R_e^2 C_e}{1+(\omega R_e C_e)^2} \qquad \textbf{Eq. 1.1}$$

Where $R_s = R_S + R_m$ is the lumped series resistance, and Z’ and Z’’ are the real (resistance) and imaginary (reactance) part of the impedance. For recording electrodes, the impedance magnitude at 1 kHz is very important since this is the characteristic frequency of a neural action potential (1 ms). For such a high frequency, Eq. 1.1 can be approximated by:

$$Z\ (j\omega) = R_s + j\frac{1}{\omega C_e} \qquad \textbf{Eq. 1.2}$$

Since $R_s << (1/\omega C_e)$ we obtain:

$$|Z|(\omega) \approx \frac{1}{\omega C_e} \qquad \textbf{Eq. 1.3}$$

Taking in consideration the Guy-Chapman-Stern theory, the electrodes capacitance is given by Equation 1.4 where C_H is the Helmholtz capacitance, ε_0 the vacuum permittivity, ε_r the dielectric constant, A the electrodes area and d_{OHP} the distance to the Outer Helmholtz Plane (Figure 1.3). Since impedance scales inversely with the capacitance, miniaturizing the electrodes area (for the design of probes with multiple micro and nanoelectrodes) would increase their impedance. [31]

$$C_H = \frac{\varepsilon_0 \varepsilon_r A}{d_{OHP}} \qquad \textbf{Eq. 1.4}$$

The design of these small electrodes that are biocompatible, highly conductive, with a high toughness, long-term resilience to the biological environment and with the desired impedance values depends on new approaches concerning their fabrication. [32] Conventional materials used to make these electrodes do not provide significantly low impedance at such scales. Therefore, there's a need in modifying these electrodes either by replacing the pristine material or by coating them with nanostructures or porous materials leading to lower impedance values and a wide range of new properties such as improved conductivity or increase charge storage capacity. [31]

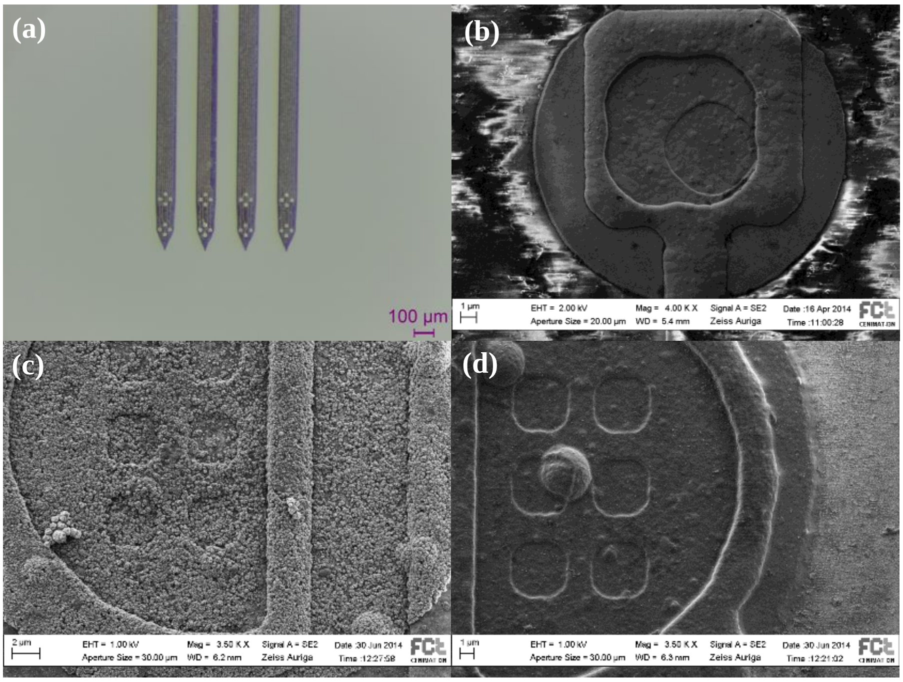

Figure 1.5 – Optical microscospe and SEM images taken of microelectrodes: (a) silicon probe (Neuronexus), (b) pristine electrode, (c) Au:PVP coated electrode and (d) PEDOT:PSS coated electrode.

2. Materials and Methods

The work abridged in this dissertation involved the synthesis and characterizations of a broad range of solutions and their electrodeposition on silicon probe's electrodes. Following the electrodeposition, electrochemical and morphological characterizations were performed. To conclude the work, neural recordings of spontaneous activity within the motor cortex were performed in anesthetized rodents to evaluate the performance of the electrode's coatings. This chapter summarizes relevant techniques used.

2.1. Solution-based synthesis

2.2.1. Commercial gold solution

Commercial non-cyanide gold solution was obtained from Neuralynx.

2.1.2. Tetrachloroauric acid solution ($HAuCl_4$) – Polyvinylpyrrolidone (PVP)

Gold solution synthesis was obtained by mixing a 25 mM tetrachloroauric acid solution (Sigma-Aldrich, 99.9%) with polyvinylpyrrolidone (20% (w/v); Sigma-Aldrich, M_W = 10 000). [33]

2.1.3. Gold nanoparticles (Au NPs)

Synthesis of gold nanoparticles was done via the citrate reduction method. A solution consisting of 1 mM of tetrachloroauric acid (Sigma-Aldrich, 99.9%) was heated on a hot plate with a magnetic stirrer until it reached the boiling point. To this solution, 1% (w/v) trisodium citrate (AnalaR NORMAPUR, 100%) was added quickly and continuously stired. After the addition of the sodium citrate solution, stirring continued until the solution turned red. [34]

2.1.4. Poly(3,4-ethylenedioxythiophene) – Poly(styrenesulfonate) (PEDOT:PSS)

Initial preparation of EDOT:PSS is achieved by mixing 0.01 M of EDOT (Sigma-Aldrich, 97%, M_W = 142.18) in water and adding 0.1 M of PSS (Sigma-Aldrich, M_W = 1000000). The solution must be vigorously stirred to dissolve the EDOT. PEDOT:PSS is obtained after the polymerization process during electrodeposition.

2.1.5. Tungsten oxide nanoparticles (WO_3 NPs)

For the hydrothermal synthesis of WO_3 nanoparticles, 0.4 g of $Na_2WO_4.2H_2O$ (Fluka, 99%) was first dissolved in 8 g of deionized water with 0.15 g of NaCl (Panreac, 99.5%) and then acidified with 1 g of 5M HCl solution (Fluka, 37%). The final solution was transferred to a 23 mL PTFE chamber, set inside a stainless steel autoclave (4745 general purpose vessel, Parr) and installed in the oven (L3/11/B170, Nabertherm). The synthesis was set to 180° C during 1 hour and let cool down to room temperature inside the oven. The product of synthesis was collected by centrifugation at 3000 rpm for 2 minutes (F140, Focus instruments) and washed three times with water. Then it was left to dry at room temperature. The final solution is achieved by mixing WO_3 NPs with water (1:1 ratio) followed by filtering (Sartorius, 0.250 μm). [35]

2.1.6. Carbon Nanotubes – Sodium dodecyl Sulfate (CNTs:SDS)

For the preparation of the carbon nanotubes solution, 1.6 mg of CNTs (Multi-Wall (MW) CNTs, NANOCYL^{TM}) were added to a solution containing 0.3% (w/v) SDS (Sigma-Aldrich, 98.5%). The solution was then submitted to 45 minutes of an ultrasonic bath (Bandelin Sonorex) followed by sonication (Sonics VibraCell) for a period of 2 minutes. The final solution product was then collected by centrifugation at 4000 rpm for 90 minutes (Focus Instruments). [36]

2.1.7. Carbon Nanotubes – Poly(3,4-ethylenedioxythiophene) composite (CNTs:PEDOT)

Composite mixtures of carbon nanotubes with PEDOT:PSS were obtained by mixing the previous CNTs:SDS solution with EDOT:PSS solution at three different volume ratios, respectively: 11% (v/v), 20% (v/v) and 50% (v/v). PEDOT:PSS is obtained after the polymerization process during electrodeposition.

2.1.8. Gold Nanoparticles - Poly(3,4-ethylenedioxythiophene) composite (Au NPs:PEDOT)

Composite mixtures of gold nanoparticles with EDOT:PSS were obtained by mixing the previous gold nanoparticle solution with EDOT:PSS solution at three different volume ratios respectively: 11% (v/v), 20% (v/v) and 47% (v/v). PEDOT:PSS is obtained after the polymerization process during electrodeposition.

After the synthesis all solutions were stored at low temperatures (4 - 6 ºC) in order to prevent deterioration. Later the solutions were used for electrodeposition at room temperature.

Figure 2.1 – Picture from different solutions prepared for electrodeposition. From left to right: EDOT:PSS, tungsten oxide nanoparticles (WO_3 NPs), commercial gold solution, Au:PVP solution, gold nanoparticles solution, and carbon nanotubes solution.

2.2. Solution Characterization

2.2.1. X-Ray Diffracion (XRD)

Structural characterization of tungsten oxide powder was performed by X-ray diffraction (XPert PRO, PANalytical).

2.2.1. Dynamic Light scattering (DLS)

Hydrodynamic diameter of gold and tungsten oxide nanoparticles in water was confirmed by Dynamic Light Scattering (DLS) technique (W130i Avid Nano)

2.2.3. Scanning Electron Microscopy (SEM)

Gold and tungsten oxide nanoparticles morphology and size were confirmed by scanning electron microscopy (SEM-FIB, Zeiss Auriga).

2.2.4. Energy-dispersive X-ray Spectroscopy (EDS)

Elemental analysis and chemical characterization of the electrode coatings was performed by energy-dispersive x-ray spectroscopy (SEM-FIB, Zeiss Auriga).

2.3. Silicon Probes

Silicon probes (polytrodes from Neuronexus) with different configurations were used (Appendix Section A):

- One shank: 16 electrodes with a diameter of 30 μm;
- One shank: 32 electrodes with a diameter of 15 μm;
- Two shank: 8 electrodes per shank presenting a tetrode configuration - in total 16 electrodes with a diameter of 20 μm;
- Four shank: 8 electrodes per shank presenting a tetrode configuration - in total 32 electrodes with a diameter of 20 μm;
- Eight shank: 4 electrodes per shank presenting a tetrode configuration - in total 32 electrodes with a diameter of 20 μm.

2.3.1. Silicon probe characterization

Prior to surgery, all electrode arrays were evaluated in terms of morphological and electrochemical performance.

2.3.2. Electrochemical characterization

A Gamry Instruments Potentiostat (Gamry Instruments, Reference 3000) was used with a three electrode cell configuration where the silicon probe's electrodes were connect as the working electrodes, a platinum wire served as counter electrode and an Ag/AgCl wire as the reference electrode. Every microelectrode was characterized in a phosphate buffered saline solution (PBS 1x) by electrochemical impedance spectroscopy (EIS) (1 MHz to 1 Hz) and cyclic voltammetry (CV) (voltage range from -0.2 to 0.8 V, $\nu = 0.1$ V s^{-1}). The fitting of the impedance spectra was carried out using Gamry Echem Analyst software by testing different models for each solution. All electrochemical data was then compared to pristine (non-modified) microelectrodes and also between different coatings. Moreover, NanoZ (Neuralynx) was used to measure impedance at 1 kHz with a two electrode cell configuration – probes were connected as working electrodes and the reference electrode was an Ag/AgCL wire (Science Products GmbH, E-255).

2.3.3. Morphological characterization

Assessment of electrode structural modifications was done by SEM (SEM-FIB, Zeiss Auriga) between 1 and 2 kV using a specific probe setup.

2.3.4. Electrodeposition set-up

The electrochemical depositions were done with the NanoZ hardware through a galvanostatic deposition process (constant current and varied time). Moreover, NanoZ was used with a two electrode cell configuration as shown in Figure 2.2.

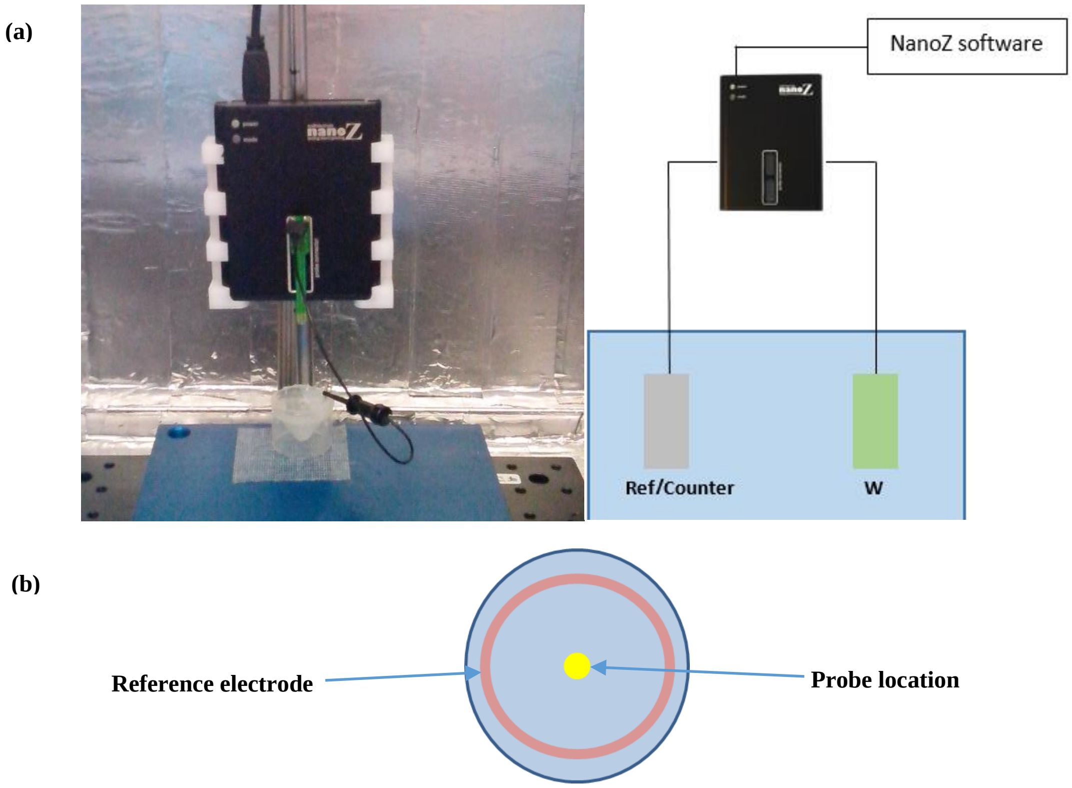

Figure 2.2 – Picture from the NanoZ with the two electrode cell deposition setup (a). The reference wire is placed around the deposition cup while the probe is maintained at a fix and equal distance to all points of the reference wire (b).

By using the ‘Manual Control’ from the software it’s possible to select individual probe electrodes. For each probe, an electrode array map must be created. Deposition process starts after selecting the deposition current.

2.4. Acute Recordings

For *in vivo* experiments we utilize anesthetized rodents (*Long Evans*) that are head-stabilized in a stereotaxic frame and receiving intraperitoneal injections to maintain an adequate depth of anesthesia during the surgery (Ketamine and Medetomidine, respectively, 1 g/10 mL and 1 mg/ml). Equipment for monitoring animal health (body temperate) as well as a video system for dorsal craniotomy and durotomy were integrated into the setup.

Anesthetized rodents undergo a surgical procedure to remove the skin and expose the skull above the targeted brain regions. An image of the exposed skull is acquired. Landmarks on the skull are then identified and used to target the brain region of interest with the help of a rat brain atlas in stereotaxic coordinates. [37] A craniotomy (4 x 2 mm) was made above the targeted brain region and the dura matter was removed to expose the brain surface where the brain vasculature, is visible. It was possible to evaluate the superficial damage that occurs during the probe insertion/extraction.

The high density electrode array silicon (Poly3-25s, Neuronexus Technologies) was then inserted to target the layer 5 of cortex. The silicon probe is on a micromanipulator that was lowered at a constant velocity (1 – 5 $\mu m\ s^{-1}$). Spontaneously neural activity was recorded from each electrode site available on the probe (32 electrodes). An open-source electrophysiology acquisition board (Open Ephys) was used along with a RDH2000 series digital electrophysiology interface chip that filter, amplify, and multiplex 32 channels (Intan Technologies). Electrodes are connected to one side of the chip, and digital data streams out the other side after analog-to-digital conversion with 16-bit resolution. The acquisition of extracellular traces sampled at 30 kSamples/s in a frequency band from 0.1 to 7500 Hz was performed for subsequent offline analysis.

Recordings were performed at different depths during 5 minutes using Bonsai software to record all neural data. All neural data was analyzed off-line using Python, Spikedetekt and Klustakwick (scripts on Appendix Section B). Analysis after the acquisition was made by filtering, aligning all spike events from the selected channel(s) and representing all channel traces in the correct geometric arrangement. Last surgical step is to euthanize the animal. Post-surgery, the probe must be rinsed with miliQ water and then cleaned with trypsin for a period that can vary from 45 minutes to 24 hours in order to remove tissue attached to the probe.

3. Results

3.1. Solution characterization

3.1.1. Au NPs

Au NPs morphology was evaluated via SEM. Even though some agglomerates can be seen (Figure 3.1), the nanoparticles have a spherical shape with an average diameter value close to 15 nm (14.5 ± 3.1 nm), corresponding to what is obtained through this technique in literature. [34] Additionally, by Dynamic Light Scattering (DLS), the nanoparticles dispersion was characterized with a mean hydrodynamic diameter of 13.1 ± 0.6 nm which is in accordance with SEM images.

Table 3.1 - Average diameter and standard deviation obtained by DLS and SEM images for Au NPs.

DLS diameter (nm)	SEM nanoparticle diameter (nm)
13.1 ± 0.6	14.5 ± 3.1 nm

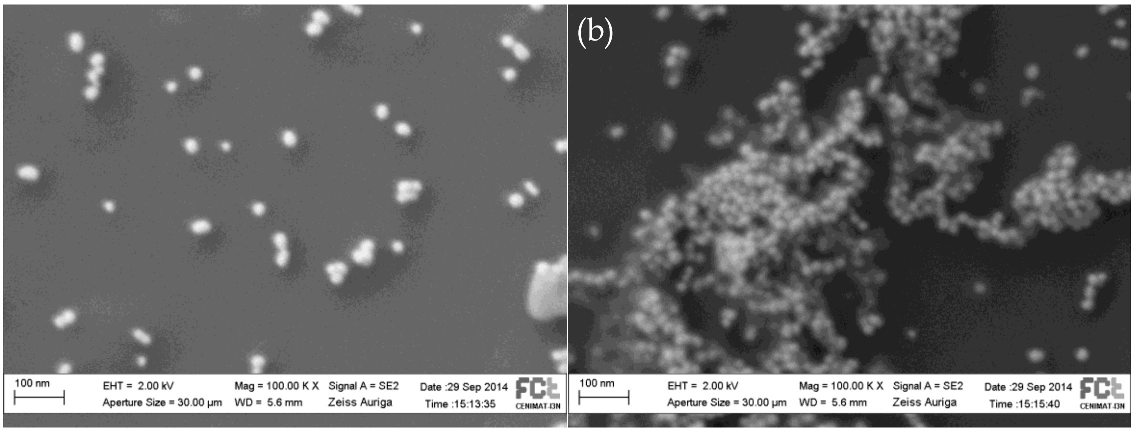

Figure 3.1 – Au NPs observed by SEM: (a) shows dispersed nanoparticles and (b) shows the presence of big agglomerates of nanoparticles.

A chemical analysis of the produced nanoparticles was performed by EDS to determine the synthesis quality. Table 3.2 and Figure 3.2 show the presence of gold (Au) corresponding to the nanoparticles and also to other chemical elements. Silicon (Si) and oxygen (O) are present due to the presence of the silicon wafer, and sodium (Na) and chlorine (Cl) appear due to the use of sodium citrate ($Na_3C_6H_5O_7$) and gold salts ($HAuCl_4$) during the nanoparticle synthesis.

Table 3.2 – EDS quantitative element analysis of average weight % and average atomic %.

	Average Weight %	Average Atomic %
O K	10.84	22.43
Na K	2.78	4.05
Si K	57.55	67.65
Cl K	1.24	1.17

Au M	27.59	4.70

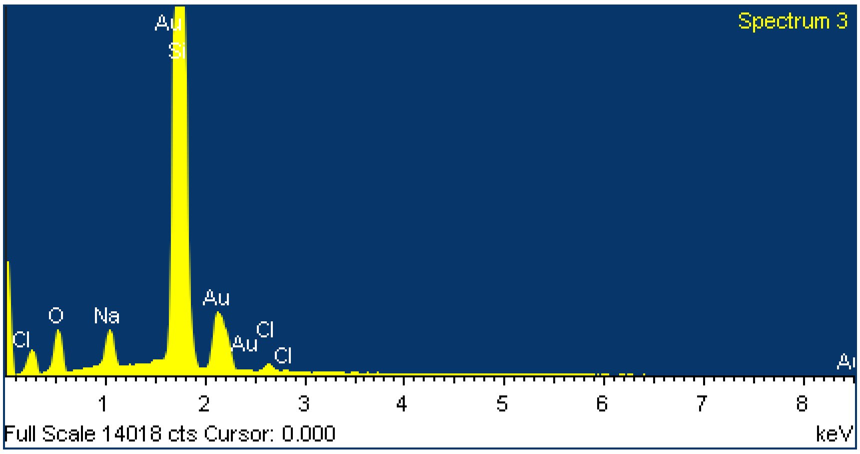

Figure 3.2 – EDS spectrum for Au NPs samples. Presence of Au NPs is evident due to the gold peaks throughout the spectrum.

3.1.2. Tungsten Oxide Nanoparticles (WO_3 NPs)

For the WO_3 NPs, the hydrothermal synthesis was chosen due to the low manufacture temperatures, easy morphologic and structural control of the nanoparticles and good reproducibility. [35] The morphology of WO_3 NPs was obtained via SEM. The nanoparticles present a non-uniform shape and are largely agglomerated to each other. The average diameter values obtained are close to 53 nm (52.69 ± 10.10 nm), corresponding to what is described in literature. [35] Also by DLS, the nanoparticle dispersion was characterized with a mean hydrodynamic diameter of 51.57 ± 6.91 nm which is in accordance with SEM images (Figure 3.3).

Table 3.3 - Average diameter and standard deviation obtained by DLS and SEM images for WO_3 NPs.

DLS diameter (nm)	SEM agglomerate diameter (nm)
51.57 ± 6.91	52.69 ± 10.10 nm

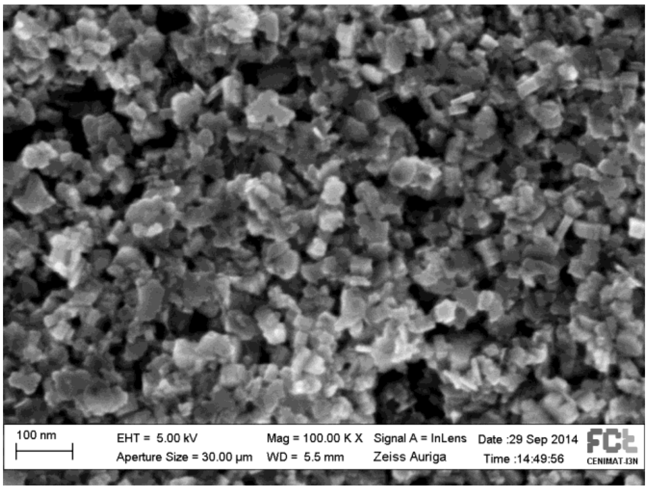

Figure 3.3 – WO_3 NPs observed on SEM.

The analysis of the chemical composition of the nanoparticles was obtained by EDS. Table 3.4 and Figure 3.4 show the presence of high amounts of tungsten (W) corresponding to the nanoparticles. Other chemical elements were also detected (Si, K, Na and Cl) due to reasons already specified above.

Table 3.4 - EDS analysis of average weight % and average atomic %.

	Average Weight %	Average Atomic %
O K	19.30	73.32
W M	80.70	26.68

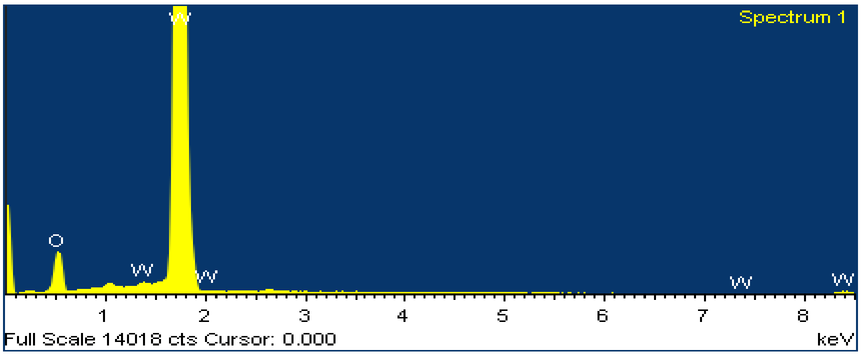

Figure 3.4 - EDS spectrum for WO_3 NPs samples. Presence of WO_3 NPs is evident due to the gold peaks throughout the spectrum.

The crystallographic structure obtained for these nanoparticles was characterized by XRD (Figure 3.5). The structure obtained can be attributed to orthorhombic hydrated tungsten oxide (ortho-$WO_3.0.33H_2O$). All diffraction peaks can be indexed to the reference pattern ICDD 01-072-0199, except in the case of the marked peaks which are probably due to structure distortion caused by the lack of total formation of the nanoparticles. This leads to a wide range of nanoparticle sizes and broad XRD peaks which are typical for structures with low crystallinity or nanocrystallinity. [35]

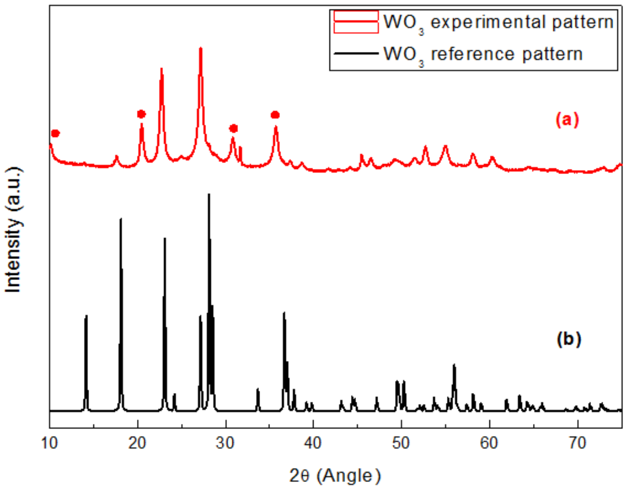

Figure 3.5 – XRD diffractograms of: (a) WO_3 synthesized powder and (b) orthorhombic $WO_3.033H_2O$ reference pattern (ICDD 01-072-0199).

3.1.3. CNTs

The morphology of the CNTs was evaluated via SEM. Hollow cylindrical shaped CNTs were observed and can be seen in Figure 3.6. The average diameter values obtained by SEM are close to 11 nm (11.08 ± 1.65 nm).

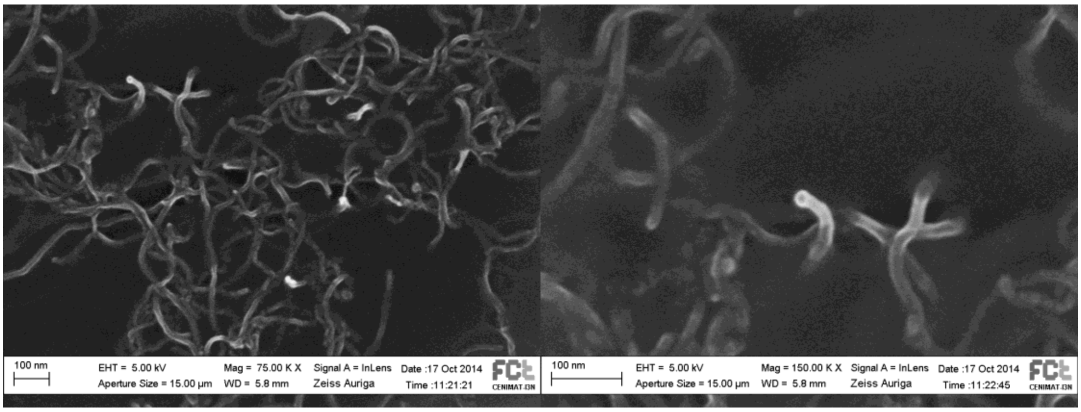

Figure 3.6 - CNTs observed by SEM: (a) shows an agglomerate of CNTs with their typical cylindrical shapes and (b) shows their hollow structure.

The analysis of the chemical composition of the CNTs was obtained by EDS. Table 3.5 and Figure 3.7 show the presence of high amounts of carbon (C) corresponding to the CNTs. Other chemical elements were also detected, with sulphur (S) and sodium (Na) being the result of the use of sodium dodecyl sulfate (SDS: $CH_3(CH_2)_{11}OSO_3Na$) as a dispersing agent for the CNTs.

Table 3.5 - EDS analysis of average weight % and average atomic %.

	Average Weight %	Average Atomic %
C K	13.59	25.07
O K	11.38	15.76
Na K	0.25	0.24
Si K	74.36	58.65
S K	80.70	26.68

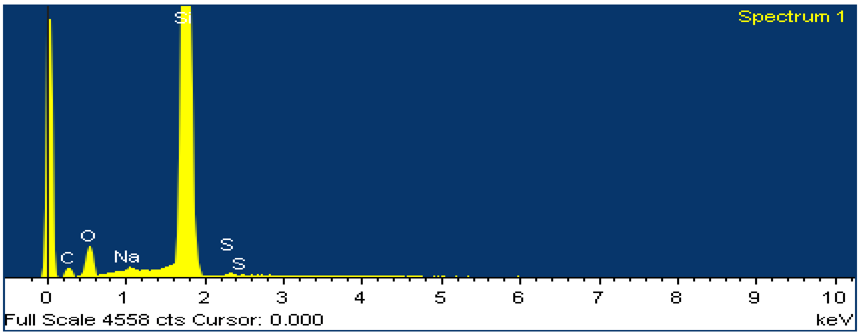

Figure 3.7 - EDS spectrum for CNT samples. Presence of C and S indicate that CNTs and SDS are present on the sample

3.2. Coating characterization

Different parameters were used in order to ascertain which would be the optimal modification to be used on the silicon probes' electrodes with the diameters presented on the previous chapter. It's known that a low deposition current would yield a poor modification of the electrode and a high deposition current value could lead to a contamination outside the electrode (consequently lead to short-circuit between them). Moreover, the impedance drop, stability over time (normally a period of a few days/to a week) and low material contamination outside the electrodes were taken into consideration.

3.2.1. Commercial Gold Solution

Commercial gold solution has been used as the standard material for coating electrodes. [38] During this work, gold deposition parameters will be assessed for future reference in order to optimize the coating process.

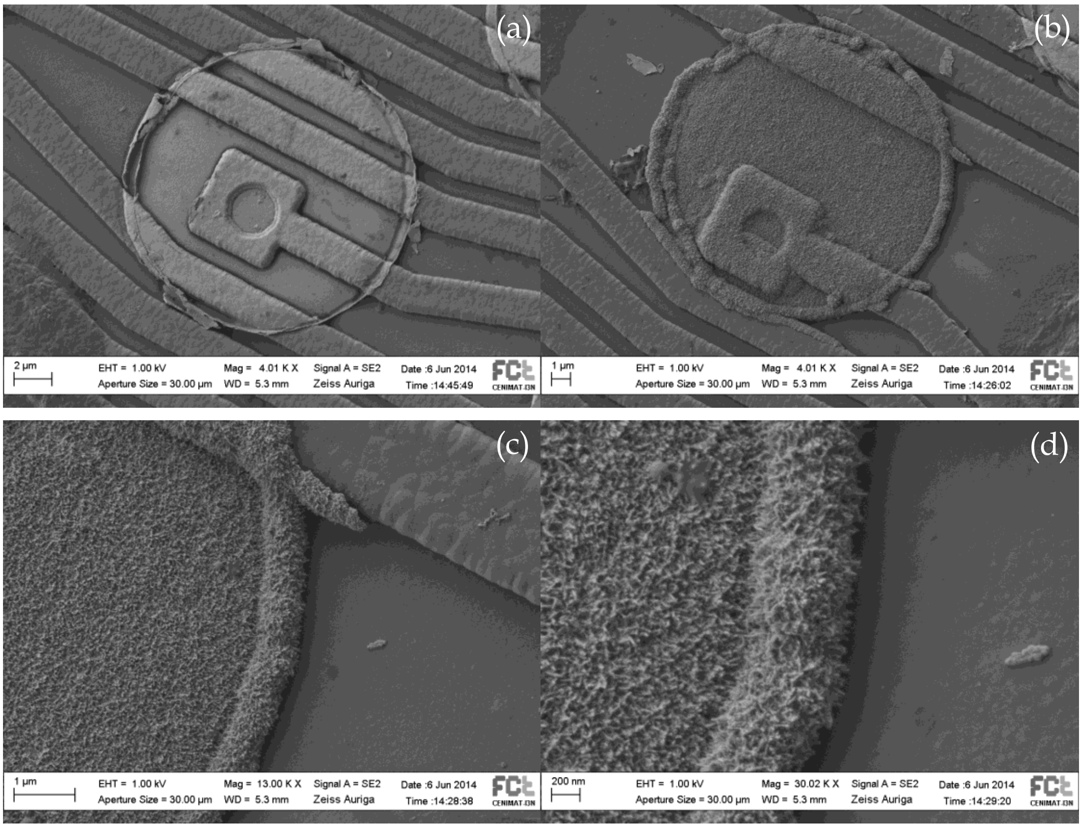

Figure 3.8 - Surface morphology of a pristine electrode on (a) and a typical gold modification on (b), (c) and (d).

Figure 3.8 shows the morphological differences between a pristine electrode and a gold coated electrode. A smooth surface is observed on Figure 3.8 (a) (pristine electrode) while a more rough surface is seen on Figure 3.8 (b) (gold coated electrode). This increase in surface area is one of the key aspects in lowering the impedance modulus at 1 kHz (frequency for neurons activity, action potential). The results presented on Figure 3.9 for gold coated electrodes (commercial gold solution) show a change in impedance (lower impedance values by increasing deposition times) and charge storage capacity (higher charge storage capacity by increasing deposition times). Different behaviors/ electrochemical performances were observed for the different deposition times which will be discussed in detail.

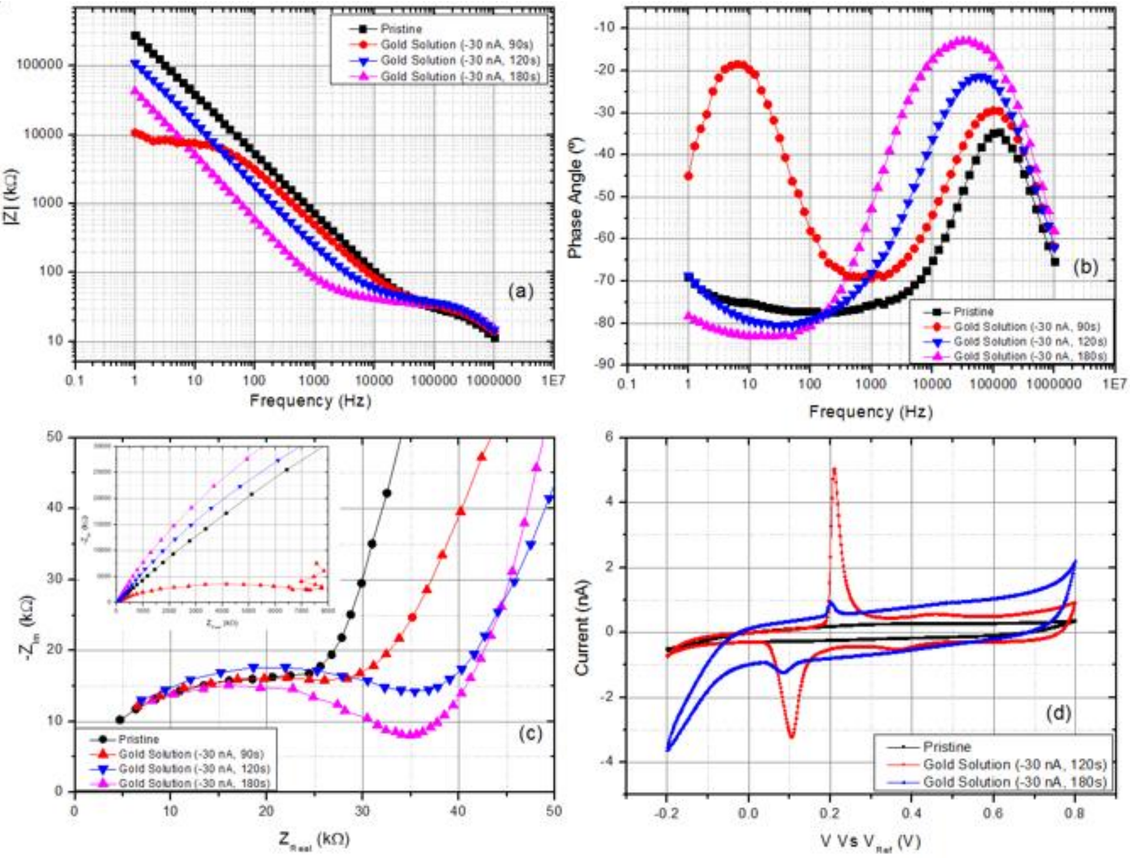

Figure 3.9 - Electrochemical characterization of non-modified and modified electrodes (with commercial gold solution): (a) EIS, (b) phase angle, (c) Nyquist plot and (d) CV.

At high frequencies (between 10 kHz and 1 MHz) the modified electrodes presented phase angle values closer to 0º (φ = 0º (resistive) and φ = -90º (capacitive)) (Figure 3.9 (b)) and an increased semi-circle (Figure 3.9 (c)) that is proportional to the deposition time. This means that the coated electrodes prolong their kinetic behavior to a broader range of frequencies affecting therefore the impedance values. A close analysis of the semicircle's dimensions shows a reduction on their length with increasing deposition time, meaning the total charge transfer resistance of the electrode decreases leading to a reduced impedance modulus (seen on Figure 3.9 (a)). Succeeding the semi-circles, the charge transfer boundary is followed by a 45º line meaning that the system is under diffusion control (the kinetics of the charge transfer at the electrode-electrolyte interface are much faster than the diffusion of ions in the solution). Figure 3.9 (c) shows a different behavior for a 90 second deposition that can also be observed on Figure 3.9 (b)) exhibiting two maxima in the phase-shift (two time constants), one for low frequencies (between 1 and 10 Hz) and the other for higher frequencies (between 100 kHz and 1 MHz). This behavior disappears for longer deposition times and combining it with the fact that the coatings for this solution are only possible after a period of 60 seconds (at least for the studied silicon probes with iridium electrodes) means that depositions below 90 seconds aren't ideal for coating these electrodes. The response given at 1004 Hz shows that an electrode coating with a 180 second deposition (-30 nA) yields a lower impedance value. Though this may seem as the ideal parameters to obtain a higher impedance drop, a higher structural instability is attained meaning that the structures formed on top of the electrodes tend to deteriorate in a short period of time leading to an increase in the impedance value.

The electrochemical stability of these gold coatings was evaluated by CV (cycle number 3 was used in total of 7 cycles) and a higher overall capacity was achieved for depositions with higher times. The highest capacity obtained (total area under the CV curve calculated on Echem Gamry Analyst) was 6.65 mC/cm^2 (11.7 nF) for a 180 second deposition which corresponds to approximately 3 times the capacity of a pristine electrode. The characteristic redox peaks indicating the presence of gold on the electrodes are seen at approximately 50 mV and 200 mV. [39] The data presented on Table 6.1 and Figure 6.2 (Appendix Section C) shows the variation in impedance before and after deposition, also taking in consideration the impedance values one day after deposition in order to assess stability of the coatings and, charge storage capacity for each coating.

3.2.2. Au-PVP

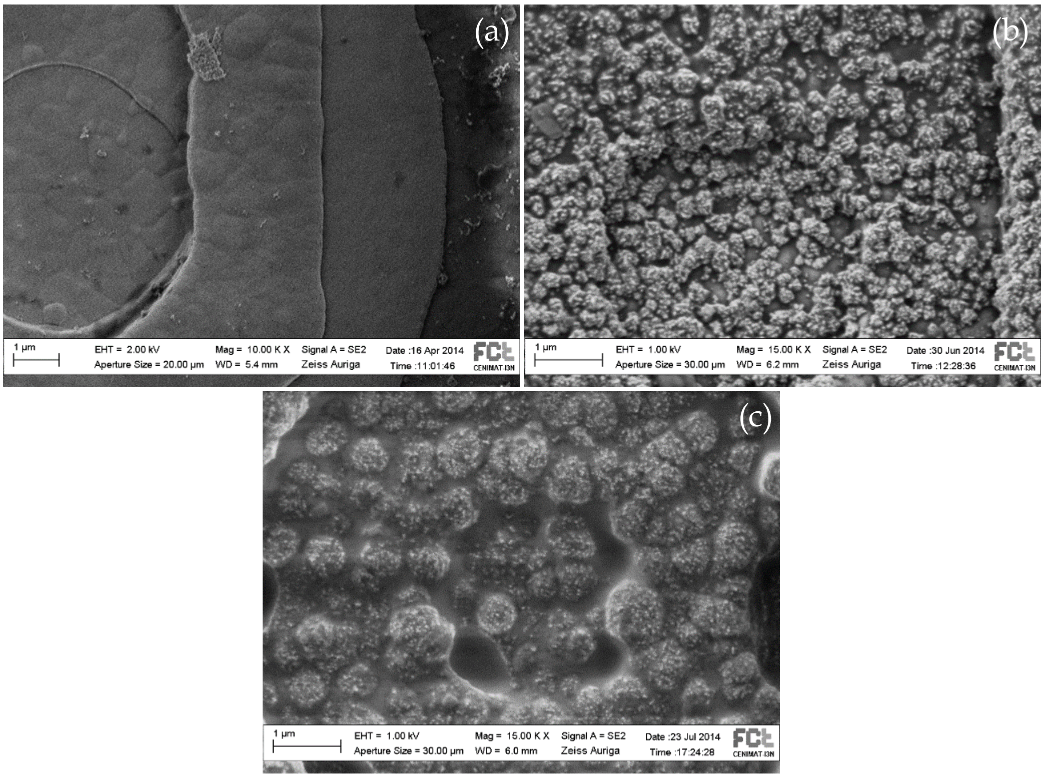

Figure 3.10 - SEM images for: (a) pristine electrode, (b) modified with Au-PVP (-30 nA, 120 seconds) and (c) modified with Au-PVP (-30 nA, 180 seconds).

The optimal parameters obtained for the Gold-PVP solution were -30 nA during a continuous deposition of 120 seconds. A lower deposition time (30 seconds) wouldn't be enough for the formation of nanostructures and for the complete coverage of the electrode. A higher deposition time (180 seconds) would yield in the agglomeration of gold disenabling the formation of nanostructure (Figure 3.10). Also, longer deposition times create a structure that stretches beyond the limits of the electrodes area which demonstrates to be highly unstable since, after one day, the electrodes impedance returns to its initial value. Moreover, the acidity of the solution (pH value of 2.5) for higher deposition times can lead to unwanted damage influencing the electrodes impedance. The morphological differences between the pristine electrode and the Au-PVP coated electrodes can be cleared observed on Figure 3.10 with a highly rough structure due to the nanostructures formed on top of the electrodes (highest increased surface area observed on Figure 3.10 (b) for a 120 second deposition).

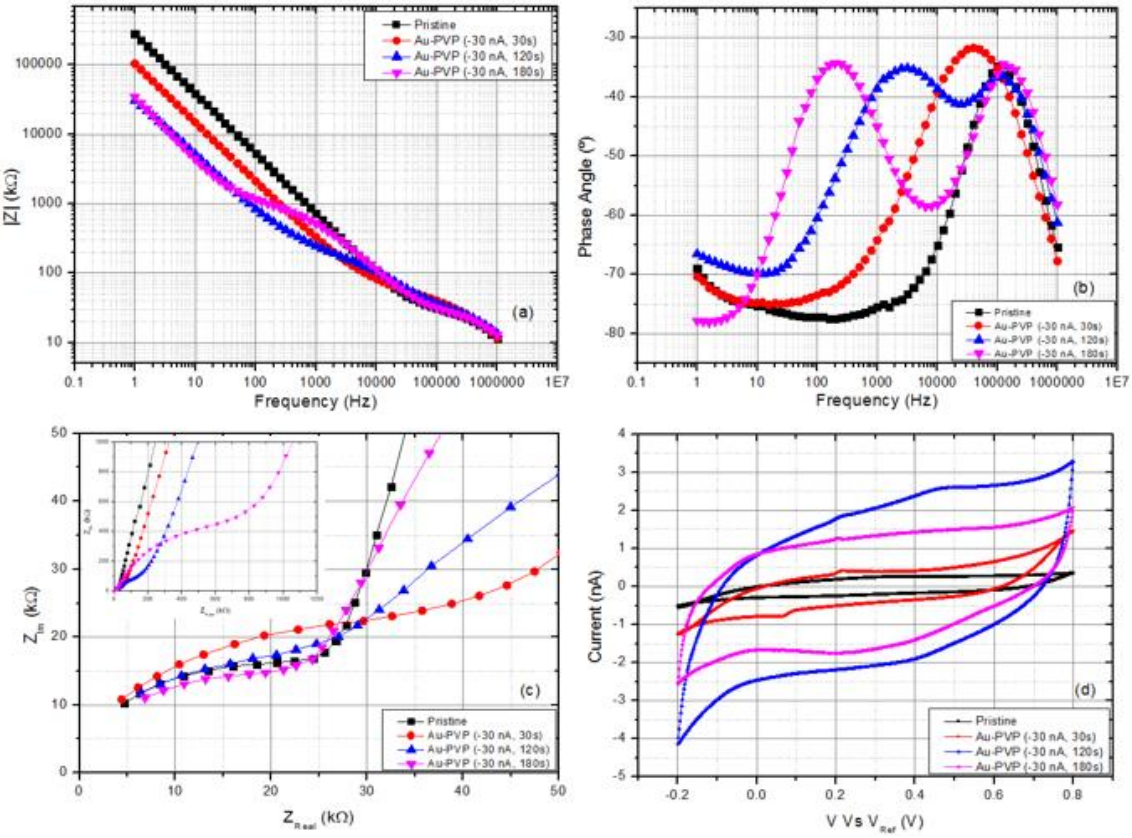

Figure 3.11 - Electrochemical characterization of non-modified and modified electrodes with Au-PVP solution: (a) EIS, (b) phase angle, (c) Nyquist plot and (d) CV.

Au-PVP coated electrodes show a similar electrochemical behavior when compared to gold coated electrodes. By increasing deposition times, the impedance magnitude decreases and the charge storage capacity increases. This is only valid up to the 120 seconds of deposition since no impedance and charge storage capacity improvements are seen beyond that value. At high frequencies (between 10 kHz and 1 MHz) the different Au-PVP coatings show a similar phase angle (Figure 3.11 (b)) corresponding to a similar initial kinetic behavior leading to identical impedance magnitude values. For higher deposition times (120 seconds and 180 seconds) two peaks (two time constants) appear on the spectra (Figure 3.11 (b)), in the mid and low frequency range (3

KHz and 200 Hz, respectively). These can also be seen in the Nyquist plots (Figure 3.11 (c)) by the display of two semi-circles.

The second peak (second time constant) may be linked with the external and porous layer formed by the Au-PVP coating. [40] Electrodes coated with the optimal parameters described previously, showed a better stability and higher overall capacity when compared to a pristine and commercial gold modified electrode. The highest charge storage capacity obtained was 19.46 mC/cm^2 (34.4 nF) for a 120 second deposition which represents approximately 9 times the capacity of a pristine electrode. The characteristic redox peaks indicating the presence of gold on the electrodes are seen at approximately 50 mV and 200 mV. The data presented on Table 6.2 and Figure 6.3 (Appendix Section C) shows the variation in impedance obtained before and after deposition, also taking in consideration the impedance values one day after deposition in order to assess stability of the coatings) and charge storage capacity for each coating.

3.2.3. Au NPs

Due to their small size (around 15 nm), gold nanoparticles are expected to yield a rugged nanostructure on top of the electrodes increasing total surface area. Several parameters were used, modifying both current and time as well as type of deposition (pulsed or continuous deposition). It was found in one hand that continuous depositions below 10 seconds resulted in low or virtually no deposition on top of the electrodes and in another hand high deposition times (above 120 seconds) would contaminate the entire probe. Therefore, small pulsed depositions were used in order to avoid the contamination. Also, the amount of nanoparticles deposited on top of the electrodes was rather small but there was a uniform distribution of nanoparticles on top of the electrodes. This way, it was possible to avoid aggregation of nanoparticles. [41,42] Morphologically, the gold nanoparticles tend to aggregate in a coral like structure on top of the electrodes increasing the total surface area.

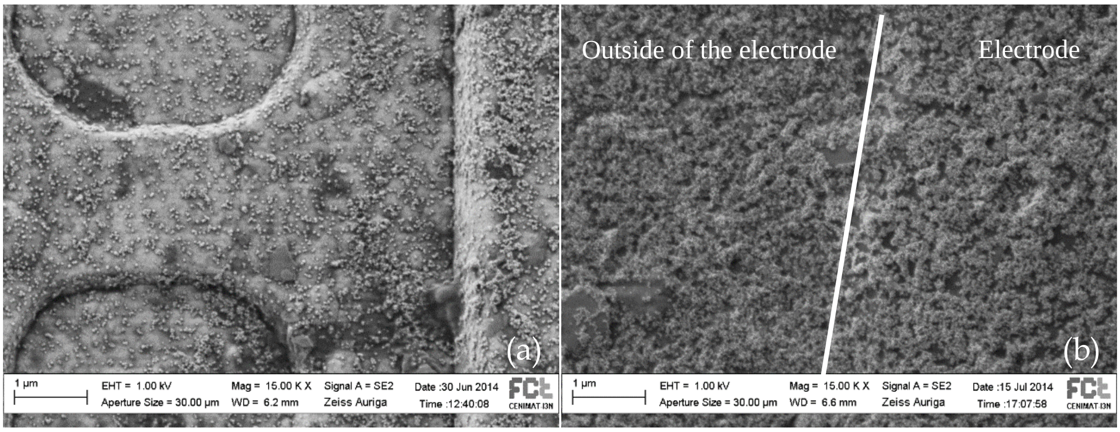

Figure 3.12 -SEM images of electrodes coated with Au NPs: (a) well distributed amount of gold nanoparticles and (b) dense distribution of Au NPs at the edge of the electrode. Contamination outside the electrode observed.

The results showed that throughout the frequency range, gold nanoparticle coated electrodes displayed a slight decrease on the impedance modulus (Figure 3.13 (a)) and an increase on the charge storage capacity (Figure 3.13 (d)).

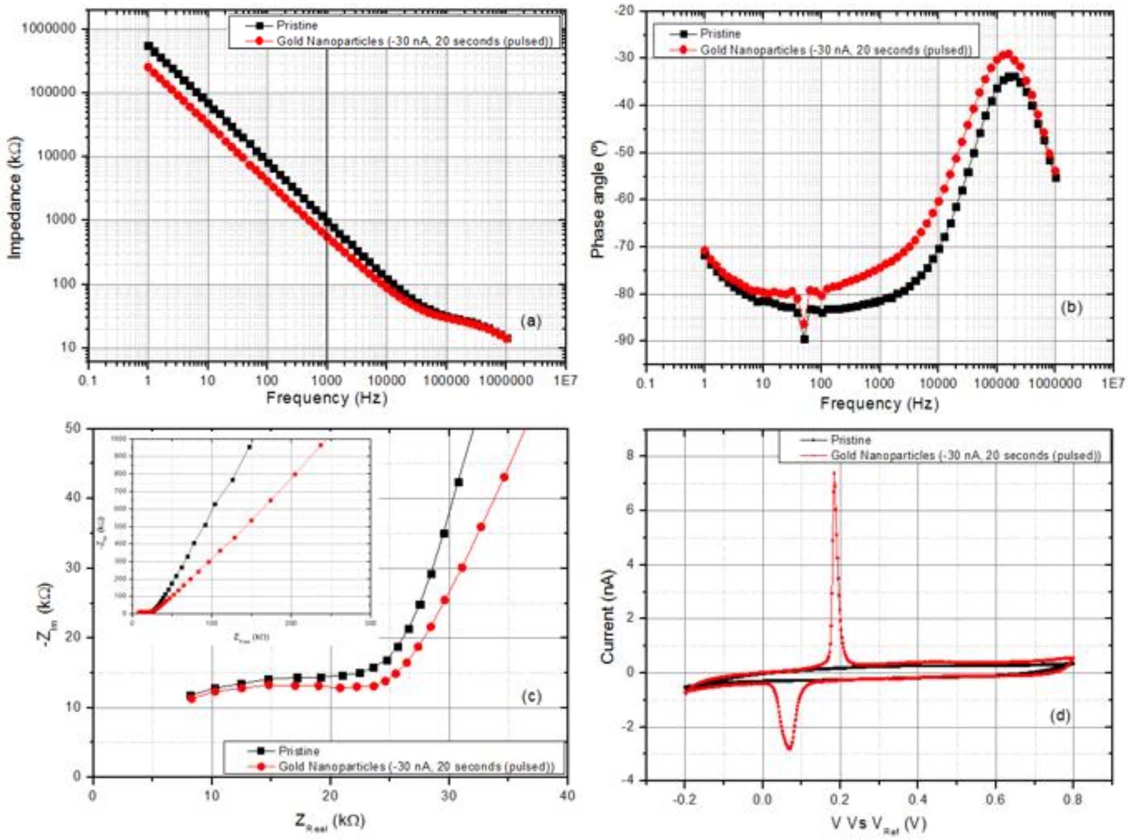

Figure 3.13 - Electrochemical characterization of non-modified and modified electrodes with Au NPs: (a) EIS, (b) phase angle, (c) Nyquist plot and (d) CV.

The slight impedance drop verified is due to the reduction of the charge transfer resistance, as seen on Figure 3.13 (c) (reduced semicircle dimension). In CV, the characteristic redox peaks indicating the presence of gold nanoparticles on top of the electrode are seen at approximately 50 mV and 200 mV, as expected. The total area of the curve had essentially no alteration when compared to a pristine electrode except for the area above and below the reduction and oxidation peaks, respectively. The value obtained for the capacity was 7.01 nF which corresponds to about 2.2 times the capacity of a pristine electrode. Though the presence of the nanoparticles can be clearly identified by SEM pictures and CV, their influence on the electrochemical properties of the electrode were insignificant. Problems with the nanoparticles adhesion onto the electrode surface could be a possible contribution to the poor performance of the Au NPs coating. A possible approach to consider is pre-treating the electrodes with UV light or submitting them to a heat treatment post-deposition. [43, 44] The data presented on Table 6.3 and Figure 6.4 (Appendix Section C) shows the variation in impedance obtained before and after deposition, also taking in consideration the impedance values one day after deposition in order to assess stability of the coatings and charge storage capacity for each coating.

3.2.4. PEDOT:PSS

Conducting polymers have been the focus of extensive studies and due to their electronic and ionic conductivity, they provide low impedance and high storage charge capacitance. [45] In addition, these materials are complemented with pseudocapacitance due to redox reactions and chemisorption processes that take place at the electrode surfaces of conducting polymers. Importantly, this kind of capacitance is faradaic in nature, rather than being associated with potential-dependent accumulation of electrostatic charge. [27]

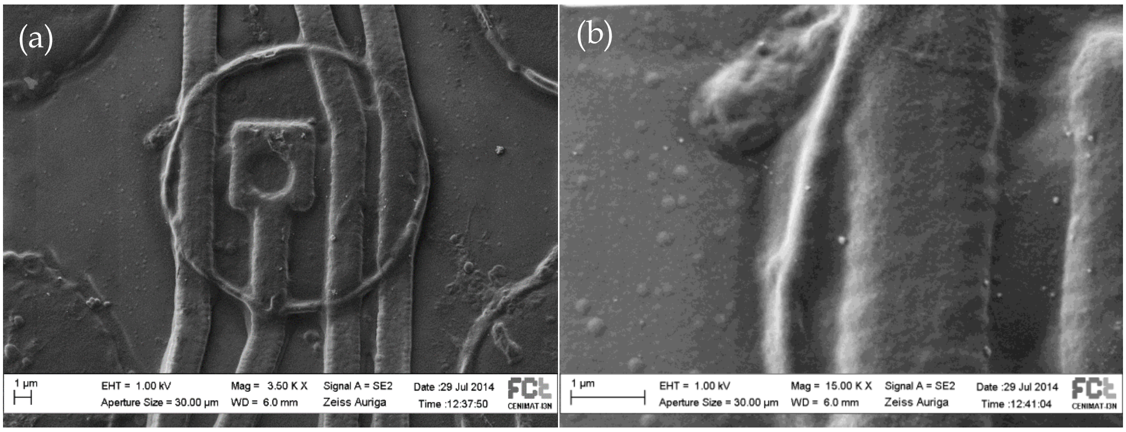

Figure 3.14 – SEM images of a PEDOT modified electrode with +30 nA for a period of 5 seconds.

Figure 3.14 shows a trans-lucid coating on top of the electrodes. Compared to metals, these conducting polymer coatings presented a relatively soft material when coated onto the electrodes surface. With the NanoZ equipment, under galvanostatic conditions, the working potential usually starts at values above +1.0 V and rapidly decreases (almost instantaneously) indicating a decline in the impedance modulus. The parameters used to provide the best coating are +30 nA for a 5 second deposition. With a deposition time of 15 seconds, there is a high probability of short circuiting nearby electrodes in these high density probes since the coating area is broader than the electrode area. So, with increased deposition time, the outgrowth of PEDOT is a factor to be taken under consideration. By lowering the deposition time to 5 seconds, it's possible to achieve lower impedance modulus drops (7% less, Appendix Section C). Since this difference is not considerably high, the 5 second protocol was adopted. By using the PEDOT:PSS coating, it was possible to achieve impedance drops by two orders of magnitude (from values as high as 1 MΩ to values as low as 20 kΩ (Figure 3.16 (a)).

PEDOT:PSS coatings showed an improvement in electrode performance both in terms of impedance magnitude (high impedance drop, between 90 and 100%) and charge storage capacity (about 17 times more charge storage capacity). At high frequencies (between 10 kHz and 1 MHz) the data obtained from a deposition of 15 seconds and 5 seconds are fairly similar, as seen on Figure 3.15. The actual changes only occur at the mid/ low frequency range (1 Hz and 1000 Hz) where a longer deposition causes a higher impedance drop on the electrodes. This difference is due to the formation of a higher coating area on top of the electrodes due to the longer polymerization time.

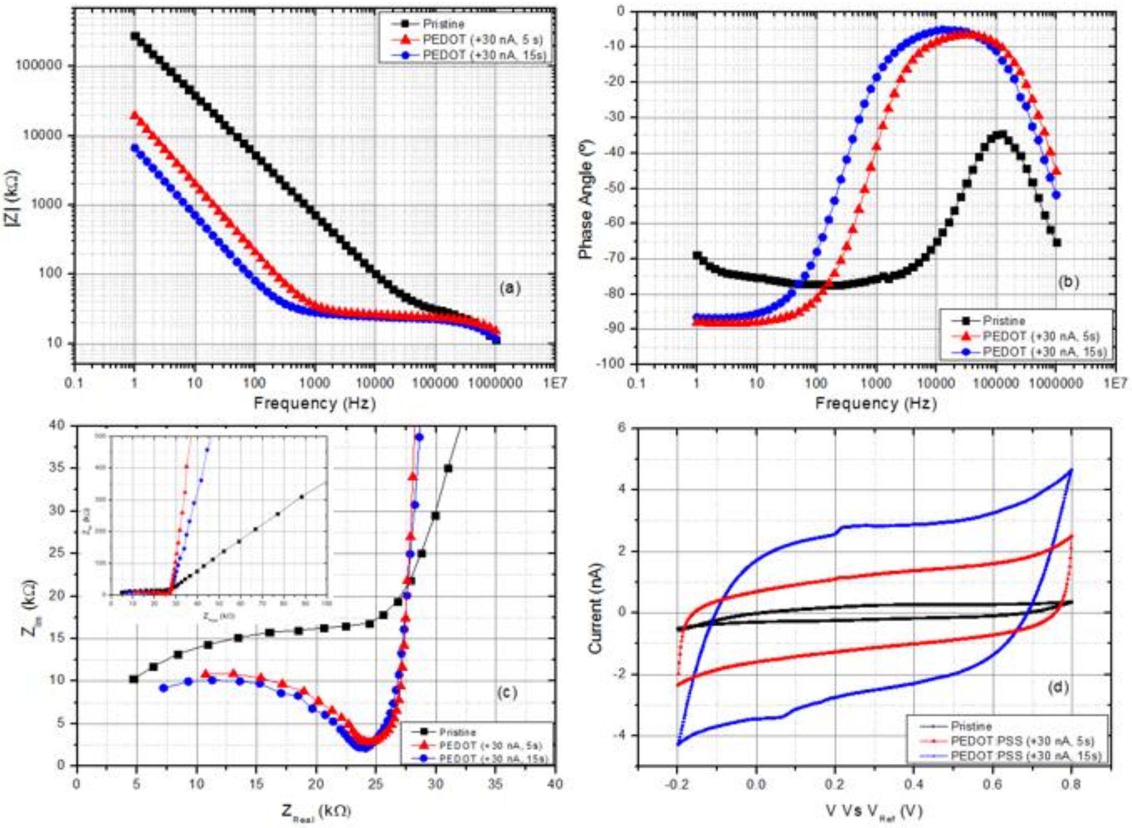

Figure 3.15 - Electrochemical characterization of non-modified and modified electrodes with PEDOT/PSS: (a) EIS, (b) phase angle, (c) Nyquist plot and (d) CV.

The behavior seen on the Nyquist plots (Figure 3.15 (c)) represents a system with an initial kinetic behavior followed by a diffusive regime. In the transition regime into the diffusive behavior, the charge transfer resistance is higher for the lower time deposition which is consistent with the smaller drop in impedance. Since these values only differ slightly, they are both considered a high and stable improvement over the pristine electrodes. Charge capacity increased with higher deposition times as expected and the highest value obtained was 36.44 mC/cm^2 (44.1 nF) which corresponds to about 17 times the capacity of a pristine electrode. Table 6.4 and Figure 6.5 (Appendix Section C) show the variation in impedance obtained and charge storage capacity for each coating.

3.2.5. PEDOT – Au NPs composite

An increase in charge storage capacity (of 1 order of magnitude) and a decrease in the impedance magnitude at 1 kHz (2 orders of magnitude) has already been shown for PEDOT:PSS coatings. By adding nanoparticles to their surface, the total electrode area is likely to increase. From Figure 3.16, it’s possible to see the presence of nanoparticles on the PEDOT:PSS matrix. Different gold nanoparticle concentrations were used (as seen on the previous section, Materials and Methods) and it was concluded that a low ratio of gold nanoparticles:PEDOT needs to be used in order to avoid nanoparticle agglomeration and allow the polymerization process for PEDOT. The visible increase in surface area (dispersed agglomerated nanoparticles add roughness to the surface) was expected to yield a higher charge storage capacity.

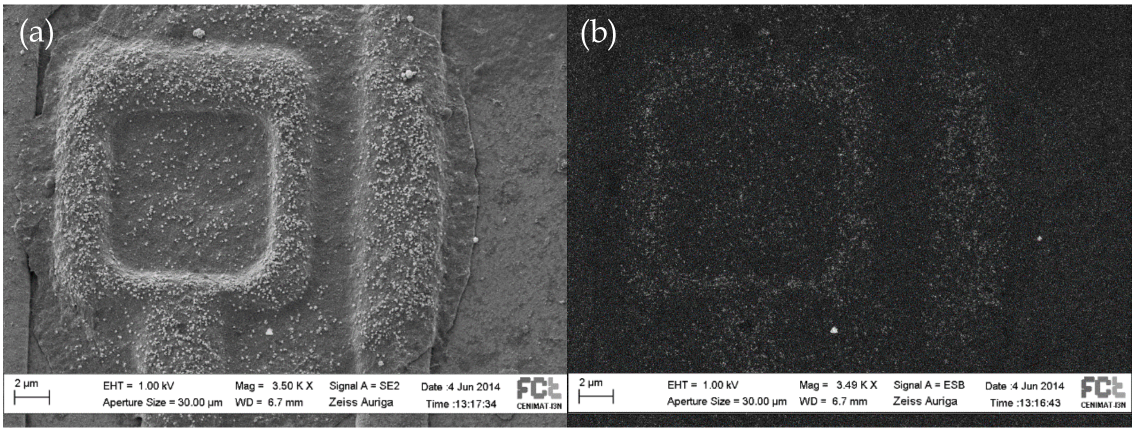

Figure 3.16 – SEM images of electrodes modified with PEDOT and Au NPs: (a) PEDOT:Au NPs coated electrode and (b) backscattered electron image showing gold nanoparticles clusters on top of the metal lines.

Electrochemical characterization showed that by adding Au NPs to PEDOT:PSS the overall charge storage capacity increases even though the impedance drop at 1 kHz was not significant (lower impedance drop than for a PEDOT:PSS coating).

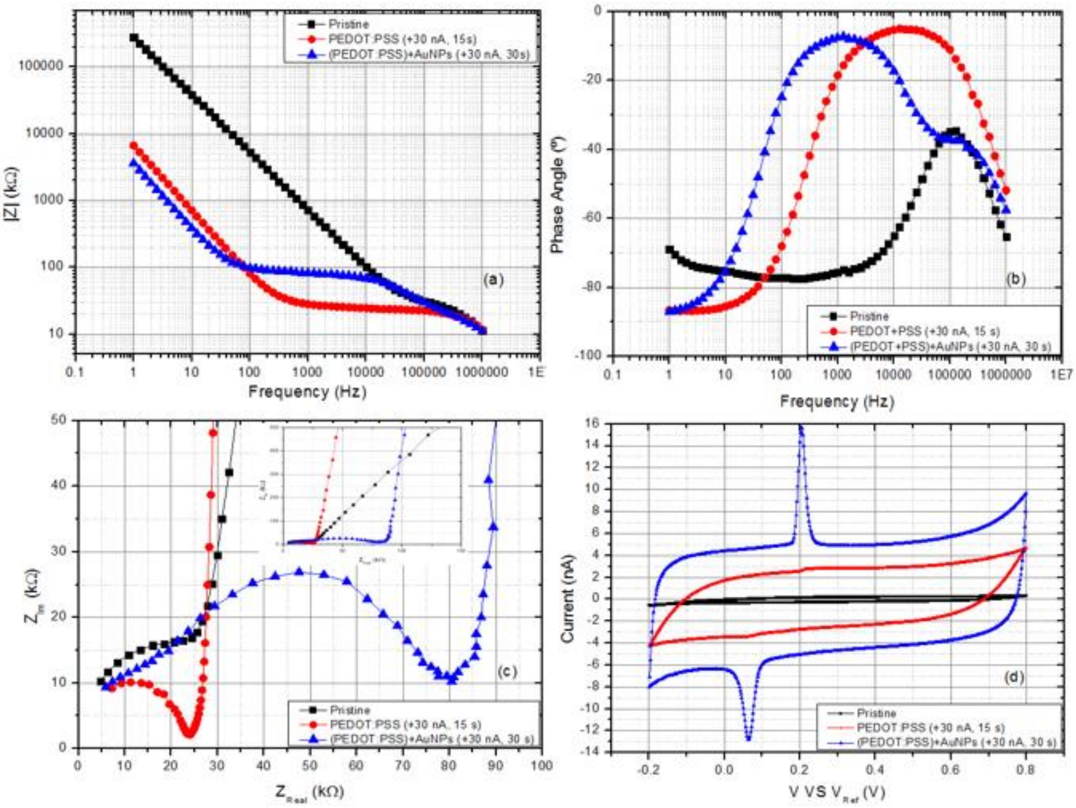

Figure 3.17 - Electrochemical characterization of non-modified and modified electrodes (with PEDOT:PSS and Au NPs): (a) EIS, (b) phase angle, (c) Nyquist plot and (d) CV.

For high frequency values (between 10 kHz to 1 MHz) the presence of these nanoparticles influences the electrochemical behavior of the electrodes. Figure 3.17 (c) shows the presence of a very large semicircle on the high frequencies range for PEDOT:Au NPs coated electrode which represents an increase on the charge transfer resistance. This will be reflected in higher impedance values when compared to a PEDOT:PSS coating (Figure 3.17 (a)). This is probably due to the presence of the gold nanoparticle clusters on the PEDOT matrix acting as a charge transfer barrier. [46] In Figure 3.17 (d), the electrochemical stability was tested and during each cycle the coating would undergo reduction and oxidation reactions corresponding with movement of ions from in or out of the coating. The characteristic redox peaks indicating the presence of gold nanoparticles on the electrodes are seen at approximately 50 mV and 200 mV. The total area under the CV curve shows that the nanoparticles on the PEDOT matrix increase the total charge storage capacity. The highest value obtained was 84.06 mC/cm^2 (101.71 nF) which corresponds to about 38 times the pristine capacity value. Table 6.5 and Figure 6.6 (Appendix Section C) show the corresponding impedance drops obtained and charge storage capacities.

3.2.6. PEDOT:PSS – Carbon Nanotubes composite

Carbon nanotubes (CNTs) have been successfully used to modify neural electrodes previously [47]. By adding CNTs to a PEDOT matrix, an enhancement of the surface area of the electrode is expected. Figure 3.18 shows the effect of the CNTs presence on the PEDOT structure.

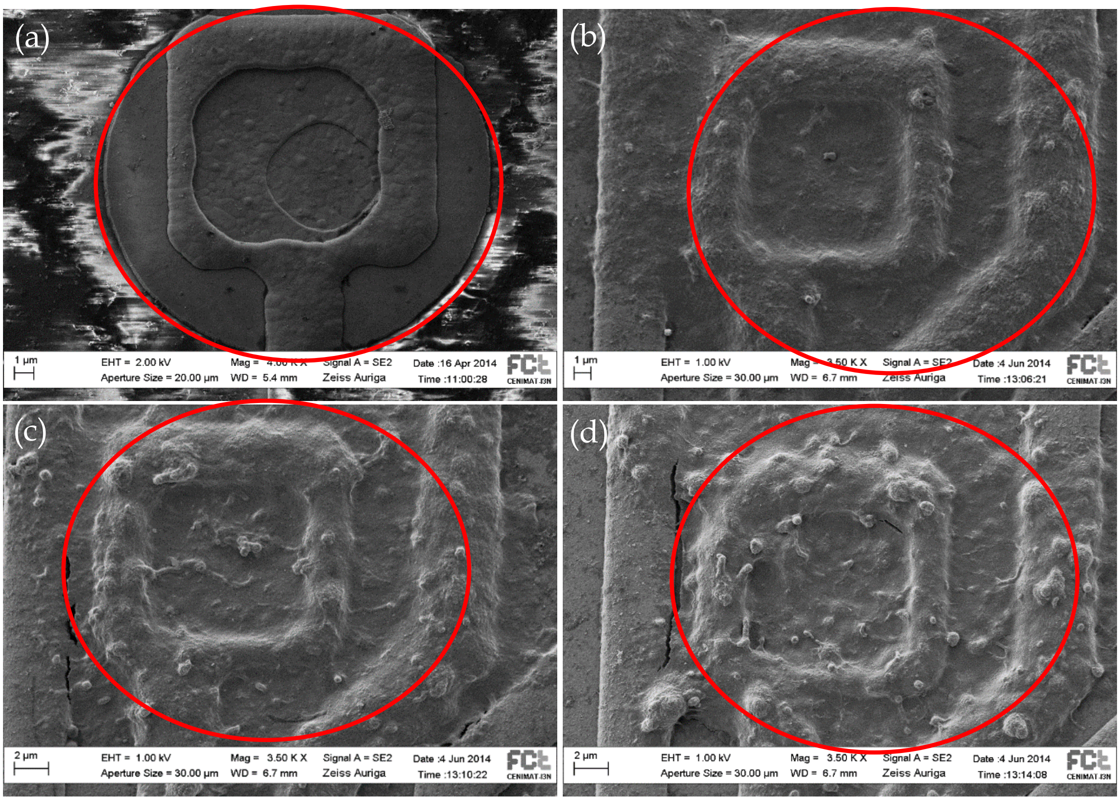

Figure 3.18 - Scanning electron microscopy (SEMFIB, Zeiss Auriga) images of electrodes modified with PEDOT:CNT composites: (a) pristine electrode, (b), (c) and (d) PEDOT:CNT modified electrodes with different concentration of CNTs: 11% (V/V), 20% (V/V) and 47% (V/V), respectively. Electrode area shown in red.

As concentration of CNTs increases (Figure 3.18), their agglomeration on the PEDOTs surface also increases. The optimal parameters for the deposition of this coating were +30 nA for a period of 30 seconds. The deposition parameters were maintained constant in order to study the influence of the concentration of CNTs.

Figure 3.19 shows that the electrochemical behavior of PEDOT:CNTs composite coatings differs from those previsouly analysed (PEDOT:PSS and PEDOT:AuNPs composite). On the low frequency range (below 10 Hz) the effect of the CNTs is neglected due to the impedance modulus being similar to the PEDOT:PSS coating (Figure 3.19 (a). Nyquist plots (Figure 3.19 (c)) show that the concentration of CNTs is directly proportional to both the size of the semicircle and the tilting of the vertical lines that appear after them. A higher concentration of nanotubes will have an increased charge transfer resistance inhibitting a decrease in the impedance modulus for higher frequencies (Figure 3.19 (a). The results suggest that CNTs behave as a charge transfer barrier. The CV curves (Figure 3.19 (d)) show that lower concentrations of CNTs will yield higher charge storage capacity. The highest charge storage capacity value obtained was 62.23 mC/cm^2 (75.3 nF) which corresponds to 28 times the value for a pristine electrode. Table 6.6 and Figure 6.7 (Appendix Section C) show the corresponding impedance drops obtained and charge storage capacities.

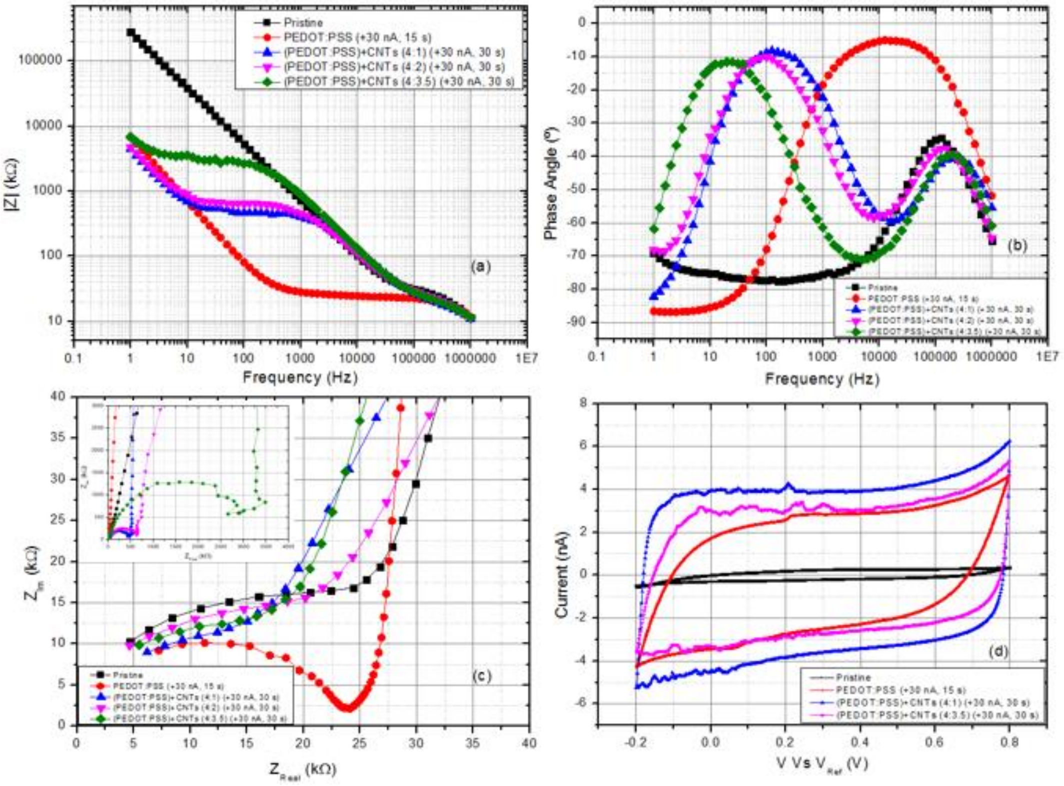

Figure 3.19 - Electrochemical characterization of non-modified and modified electrodes with PEDOT:CNT composite: (a) EIS, (b) phase angle, (c) Nyquist plot and (d) CV.

3.2.7. WO_3

Semiconducting oxides are amongst the most widely studied materials with interest being driven both by the fundamental challenges posed by their electronic and magnetic structures and properties, and by the wide range of applications. Tungsten oxide has shown very promising properties especially in the form of nanostructures with large surface area due to the wide band gap typical of this material and its high stability. [35]

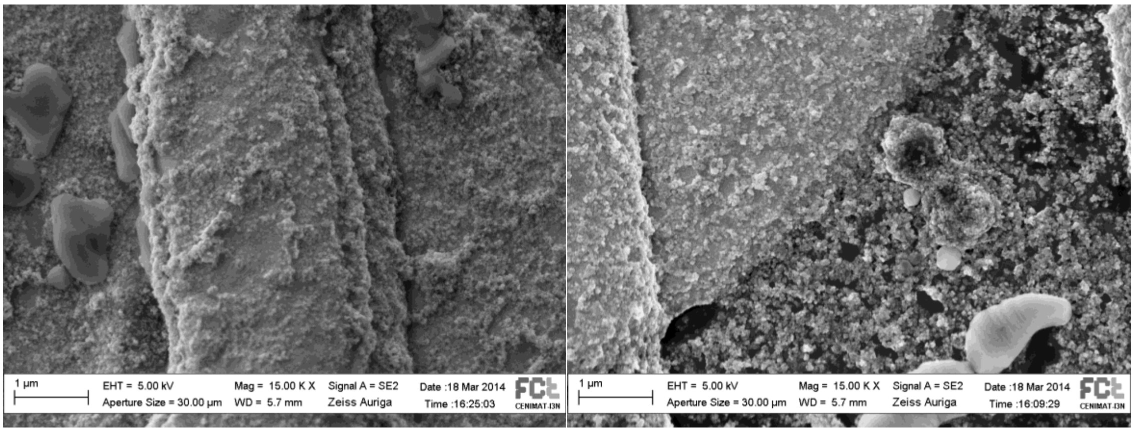

Figure 3.20 -SEM images of electrodes coated with WO_3NPs: (a) deposited near a metal line and (b) dense distribution of WO_3 NPs at the edge of the electrode. Contamination outside the electrode observed.

Taking into consideration the work done by [35], tungsten oxide nanoparticles were able to lower the impedance value of gold electrodes (1 mm^2). Similar to what was completed on the previous paper, the same protocol was performed in this thesis in order to create a WO_3 nanostructure on top of the electrodes. Moreover, the possibility of taking advantage of the pseudocapacitive effects of tungsten oxide is also evaluated. [48] Figure 3.20 shows that a WO_3 NPs structure was formed onto the electrodes but with a high contamination on the insulating area outside the electrodes (deposition time of 120 seconds with -30 nA).

The results obtained on Figure 3.21, show that throughout the frequency range, impedance and phase angle values remained fairly similar to the pristine electrode. As previously reported [35], heat treatment after nanoparticle deposition could increase the adhesion to the electrodes surface. Since the electrodes on these probes are made of iridium (which will oxidize fairly easily when submitted to a heat treatment) there’s a need in placing them under vacuum conditions for any pre or post deposition treatments involving temperature. On the cyclic voltammetry curve (Figure 3.21 (d)), the total area under the curve had virtually no alteration when compared to a pristine site. No significant increase on the charge storage capacity was obtained. Table 6.7 and Figure 6.8 (Appendix Section C) show the corresponding impedance drops obtained and charge storage capacities.

Section D shows a table (Table 6.8) with the summary of all the best results obtained.

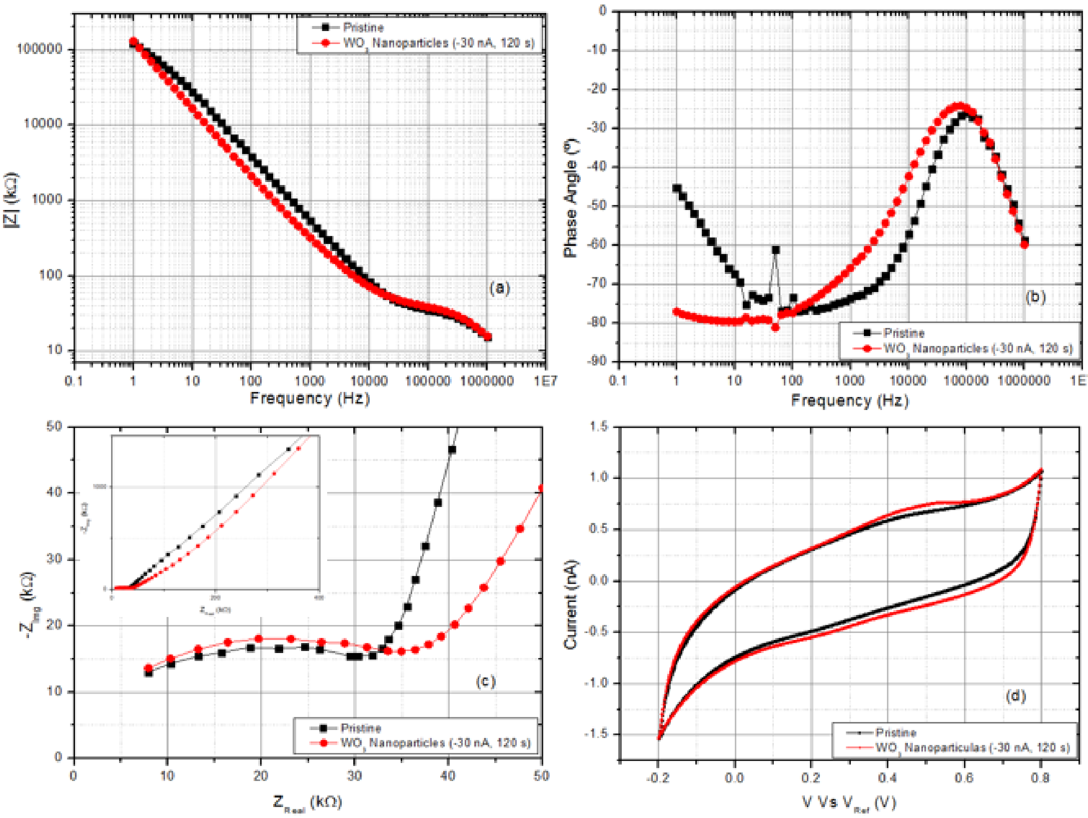

Figure 3.21 - Electrochemical characterization of non-modified and modified electrodes (with WO_3 NPs): (a) EIS, (b) phase angle, (c) Nyquist plot and (d) CV.

3.3. Equivalent circuit modelling: Electrode-Coating-Electrolyte Interface (ECEI)

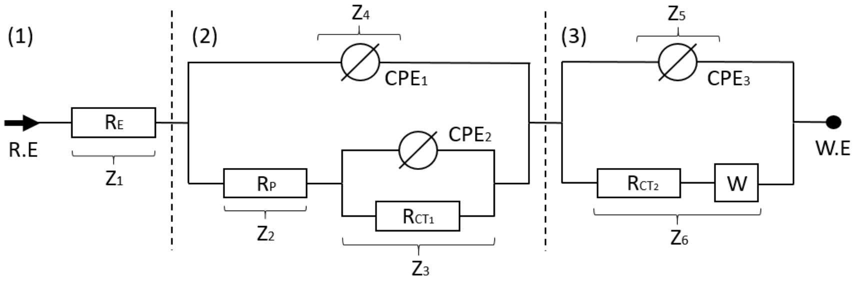

Figure 3.22 - Electrode-coating-electrolyte interface components scheme: (a) shows the representation of the impedance of the coating-electrolyte interface and (b) shows the equivalent circuit used to fit the impedance spectra.

Figure 3.22 shows the equivalent circuit that had the better fit for the data. The model is divide in 3 components from the reference electrode (R.E) to the working electrode (W.E): (1) corresponds to an uncompensated electrolyte resistance that models the resistance of the electrolyte seen by the electrode, R_E; (2) takes in consideration the nature of an imperfect coating where the electrolyte contacts the metal electrode through porous structures and, also takes in consideration grand boundaries where the behavior of the materials differs: CPE_1 a constant phase element used to model the capacitance of the coating layer, R_p is the resistance associated with defects (from the porous structure), CPE_2 a constant phase element used to model the capacitive double layer at the electrode interface, also known as the Helmholtz double layer (accounts for no-idealities due to surface inhomogeneity), R_{CT1} is the charge transfer resistance that models the resistive pathway due to electrochemical reactions and, (3) corresponds to a continuous coating not taking in account imperfections, where CPE_3 is the constant phase element used to model the capacitive double layer, R_{CT2} the charge transfer resistance and W represents the Warburg diffusion process in the metal. [49,50,51] Further work in simulation is needed in order to understand the results obtained.

3.4. Acute Neural Recordings

In order to evaluate the performance of different electrode modifications, five minute recordings of spontaneous neural activity under ketamine at different depths within the cortex were performed. The high density probe (HDP) had a deposition layout that allowed for maximum variety of coatings taking in consideration paired depositions (depositions with the same parameters and materials) in order to provide a valid comparison between nearby electrodes.

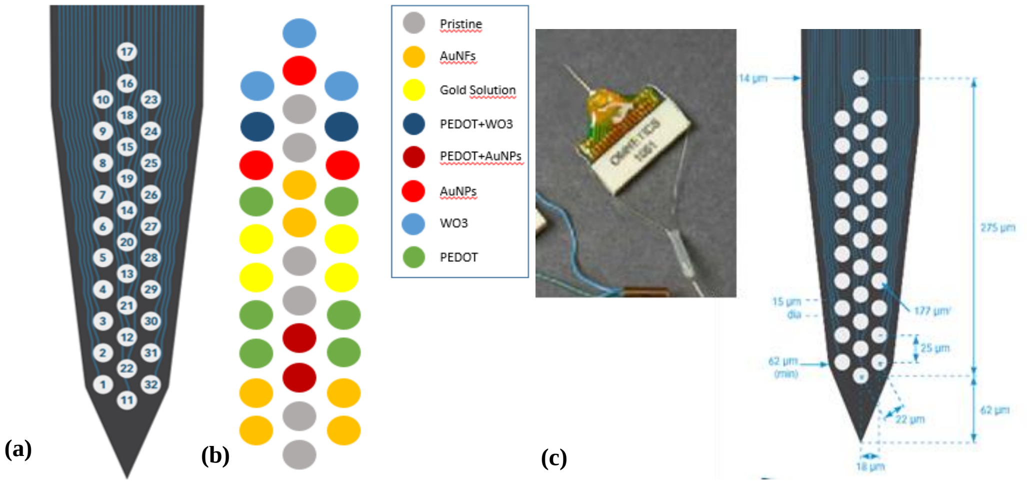

Figure 3.23 – High density 32 channel probe from Neuronexus: (a) shows the site number layout on the probe, (b) the modification layout with different materials and (c) probe image with the standards.

Throughout the experiment, higher cell activity was detected during recording number 2 (Figure 3.24). So, an extensive study of the previous recording (recording number 1) and the following recording (recording number 3) was done in order to compare cell activity for the different recordings at different depths. The neural recording ability of both coated and uncoated electrodes was evaluated by detecting spontaneous activity within the cortex, as previously stated. By moving the electrode array in the tissue, it is expected that the neural signals from the same neurons are to be collected through both the coated and uncoated electrodes. Table 6.16 (Appendix Section F) shows the data from three consecutive recordings performed at different depths and Figure 3.25 shows a piece of the data set to retrieve neuron spiking data. No significant data was obtained for WO_3NPs and PEDOT:WO_3NPs coatings throughout the recordings. This may be the result of these coatings being located on the upper electrodes of the HDP where almost no cell activity was detected during this experiment. Future recordings are necessary to further assess the *in vivo* recording capability of WO_3NP coatings.

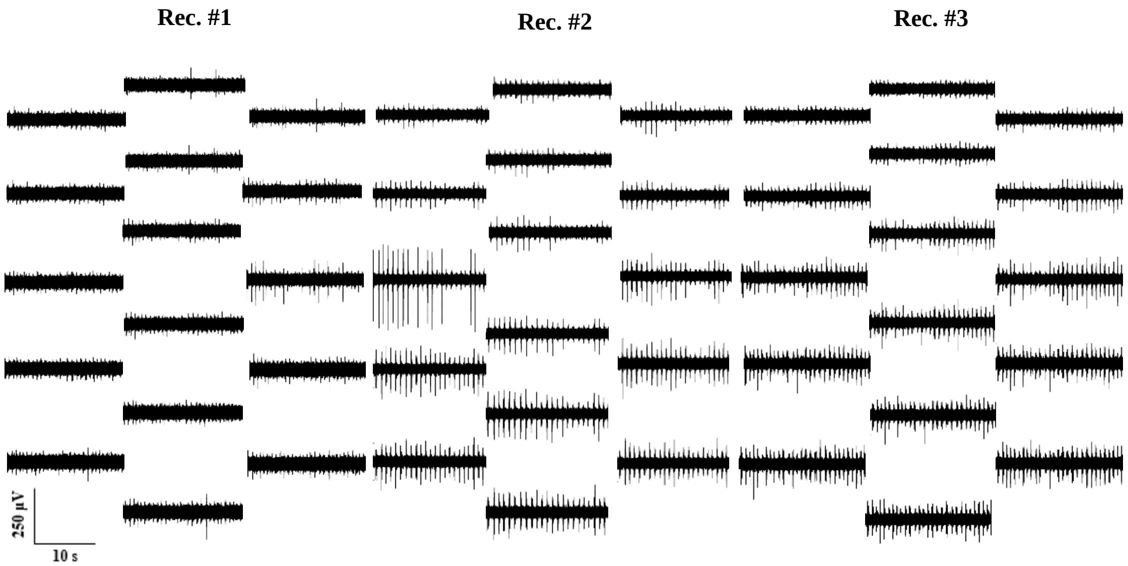

Figure 3.24 – Cell activity from multiple recordings taken from the tip of the HDP. Appendix Section G presents the location of the recordings with the corresponding brain atlas map.

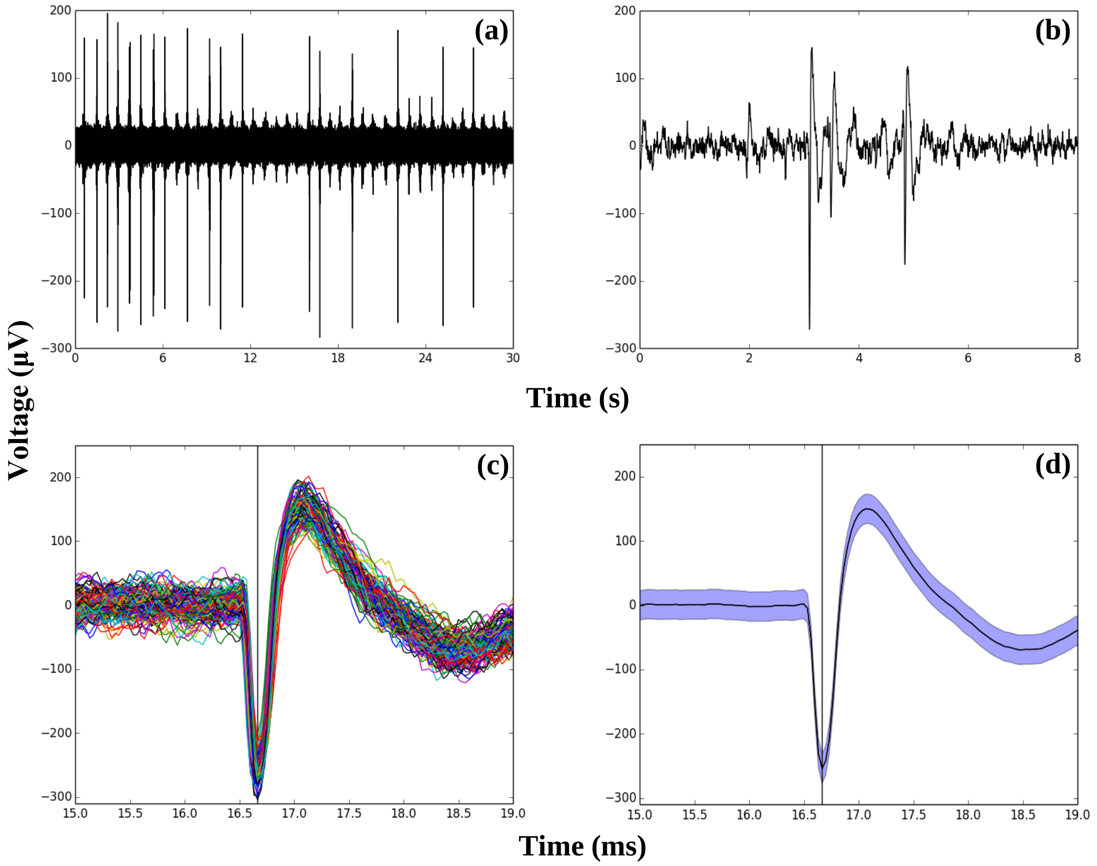

Figure 3.25 – Neural spontaneous activity within the cortex for a PEDOT modified electrode: (a) high-pass filtered data containing 30 seconds of information, (b) zoom in the filtered data, (c) and (d) spike average and standard deviation obtained after applying a voltage threshold (-100 µV).

The average peak-to-peak (P2P) amplitudes are given by averaging the maximum amplitude values obtained for similar electrodes, for example:

$$P2P_{avg}(PEDOT) = PEDOT_{MaxAmp\ 1} + \cdots + PEDOT_{MaxAmp\ X} = \sum_{i=1}^{N} PEDOT_{MaxAmp\ N}$$

$$P2P_{avg}(Electrode\ Coating) = \sum_{i=1}^{N} Electrode\ Coating_{MaxAmp\ N} \qquad \textbf{Eq. 3.1}$$

Coated electrodes show improved average P2P amplitudes with quality unit activity being evident on the modified electrodes across the HDP at every time point in this study (from highest to lowest: PEDOT:Au, PEDOT, Au:PVP, Pristine, Gold, respectively). Maximum P2P amplitude obtained was for a PEDOT coated electrode with a value of 404.37 μV on recording #2. These higher signal amplitudes obtained are related to the lowered impedance of the electrode by the deposition. Whether this decrease of impedance (increase in sensitivity) will also benefit long-term recordings needs to be tested with chronic experiments. Though gold coated electrodes seem to be underperforming when compared to pristine electrodes, previous studies have shown that gold modifications improve the *in vivo* performance of the electrodes [52] Signal-to-Noise Ratio (SNR) values are obtained through the following equation:

$$SNR = \frac{Amplitude\ P2P}{2 \times STDV} \qquad \textbf{Eq. 3.2}$$

The recorded data exhibited a SNR as great as 8.86 for a PEDOT coated electrode (compared to the maximum value of 6.05 obtained for a pristine electrode) while the average SNR across the HDP shows similar values for electrodes with PEDOT and/or PEDOT:AuNPs having the highest average values. Low impedance of the coated electrodes helped reducing noise levels allowing for the detection of lower amplitude single units (from neurons located further away from the recording electrode) which cannot be discerned on standard electrodes. The lowest noise level obtained was for a PEDOT modified electrode with a value of 19.84 μV. During the acute neural experiments, the silicon probes are subjected to mechanical strain when entering the brain. If the coatings are not stable enough and/or have a low adhesion to the surface of the electrode there is a high probability of deterioration of the nanostructures previously built on top of the electrodes. This process is inevitable and is responsible for the increase in impedance post-surgery (though, depending on the coating used, this values can remain fairly low when compared to the pristine equivalent).

4. Conclusions and Future Perspectives

Neural probes, as a tool, offer unique scientific and clinical opportunities for investigation, diagnosis, and treatment of neural conditions. Dysfunctional activity can often be identified non-invasively using neuroimaging techniques, including fMRI combined with EEG. Once localized, affected brain structures can be studied in further detail by introducing probes to analyze the neurochemistry, record the electrical activity, and stimulate either acutely or chronically. [27]

This project aimed at improving the efficiency of signal transfer from the neural tissue to the electrodes. Different electrode coatings were developed, and successful proof-of-concept acute recordings within the cortex of rodents have been demonstrated. Moreover, the electrode's coating performance was tested in saline in a variety of experimental models ranging from electrode impedance monitoring, to charge storage capacity evaluation and to long-term multi-channel acute recordings. While acute experiments are essential to validate new implantable systems, they do not represent clinically relevant chronic settings. Future experiments concerning chronic implantation should proceed this work.

The main conclusion to take from this work is that different materials (gold, PEDOT, tungsten oxide and carbon nanotubes) can be successfully used to modify high dense electrode arrays presented in commercial silicon probes in order to increase the electrodes charge storage capacity and lower the impedance modulus. Additionally, the formation or deposition of nanostructures on top of the electrodes was achieved by using the same technique through this project – galvanostatic electrodeposition. The viability of these modifications is shown through several electrochemical measurements (electrochemical impedance spectroscopy and cyclic voltammetry) and by performing acute neural recordings in rats. A wide range of deposition parameters were studied in order to have a better understanding on how the electrodes behavior would be altered and what would be the ideal coating for the different materials used. These differences in the electrodes electrochemistry lead to a change in their intrinsic properties.

Gold coated electrodes have shown the possibility of lowering the impedance magnitude (up to 1 order of magnitude) and increasing the total charge storage capacity. By adding a polymer, in this case PVP, to a gold solution, a higher surface area was obtained due to an increase of the nanostructures being formed on top of the electrodes. The Au:PVP solution allows a more rugged structure leading to a higher decrease in the impedance modulus and an increase on the total charge storage capacity when compared to the standard commercial gold solutions.

Gold nanoparticle and tungsten oxide nanoparticle coated electrodes where expected to yield a decrease in impedance by increasing the total surface area of the electrodes and ultimately increase the sensitivity of the electrodes due to their intrinsic properties. It was observed that no stable coatings were obtained through the parameters chosen and used during this work. Further studies need to be conducted in terms of nanoparticle adhesion to iridium electrodes.

PEDOT coated electrodes allow for a maximum decrease of two orders of magnitude on the impedance modulus (from 1 MΩ to 25 kΩ) while increasing the total charge capacity by one order of magnitude (from 2.2 mC/cm^2 to 36.4 mC/cm^2) for 15 μm diameter electrodes. By mixing PEDOT with gold nanoparticles and carbon nanotubes, slightly higher impedance values were obtained at 1 kHz (approximately 100 kΩ) while increasing the charge storage capacity up to a maximum of 62.2 mC/cm^2 for PEDOT:CNTs and 84.1 mC/cm^2 for PEDOT:AuNPs. Electrodes with lower impedance values may increase the recording sensitivity and possibly allow the detection of signals even in the presence of the insulating tissue surrounding the silicon probe. However, the use of CNTs and nanoparticles in neural implants also raises concerns about their pathogenic potential and exposure limits. There still exists a lack of information regarding the acute and long-term effects that CNTs and nanoparticles may have on the brain. Such issues must be addressed concomitantly to the improvement of their physicochemical properties.

Through the neural recordings, the maximum P2P amplitudes, the highest SNR and the lowest noise levels were obtained for coated electrodes when compared to their pristine equivalent (PEDOT with a P2P amplitude of 404.37 μV, SNR of 8.86 and noise level of 19.84 μV). Overall, the acute neural physiological experiments show that coated and uncoated electrodes can record neural signals within the cortex of rodents. These results demonstrated the capability of modifying pristine electrodes to record neural signals, the potential of modified electrodes in recording neural activity ranging from single units to network-wide bursts and improved performance of these electrodes which could facilitate the separation of discrete neural signals and the recognition at the cell's distinct shape. This means that probe modification is a suitable and easy way to alter electric and physical properties of silicon probes without compromising their performance.

For an actual and meaningful communication with the brain, recording and stimulation must be performed simultaneously. Although micro-fabrication has led to different concepts that allow the recording of numerous neural activities in awake animals, the quality of these recordings typically deteriorates over time: electrode performance decreases and properties vary over time. In most cases, it is still not clear what causes these variations so new methods must be employed in order to minimize problems involving biocompatibility, durability and reliability of the measurements. These may include the use of hybrid neural probes with nanostructured materials. The major challenges for *in vivo* systems are the development of real-time and specific detection algorithms, safe stimulation, minimal interference between recording and stimulation channels, and a stable electrode-tissue interface. Progress in this area relies on scientists being able to integrate and utilize methodologies from different disciplines, such as biomedical engineering, biomaterials, neuroscience, neurology, neurosurgery, information and communication technologies, molecular biology, etc. The procedures for the implantation of penetrating microelectrodes are straightforward and well within the reach of most well-trained neurosurgeons. Altogether these results suggest that the formation of nanostructures with different materials look promising in augmenting the signal transfer from the tissue to the microelectrodes and could form the basis of new neuroprosthetic devices for treating many disorders of the nervous system. The next step would be the study the long-term effects (chronic implants) of these modified microelectrode devices.

5. References

[1] Rapoport, J. L., & Gogtay, N. (2008). Brain neuroplasticity in healthy, hyperactive and psychotic children: insights from neuroimaging. *Neuropsychopharmacology : Official Publication of the American College of Neuropsychopharmacology, 33,* 181–197. doi:10.1038/sj.npp.1301553

[2] Azevedo, F. A. C., Carvalho, L. R. B., Grinberg, L. T., Farfel, J. M., Ferretti, R. E. L., Leite, R. E. P., … Herculano-Houzel, S. (2009). Equal numbers of neuronal and nonneuronal cells make the human brain an isometrically scaled-up primate brain. *Journal of Comparative Neurology, 513*, 532–541. doi:10.1002/cne.21974

[3] Nam, Y. (2012). Material considerations for in vitro neural interface technology. *MRS Bulletin*. doi:10.1557/mrs.2012.98

[4] Georgiev, D. D., Papaioanou, S. N., & Glazebrook, J. F. (2004). Neuronic system inside neurons: Molecular biologyand biophysics of neuronal microtubules. *Biomedical Reviews*.

[5] Buzsáki, G., Anastassiou, C. A., & Koch, C. (2012). The origin of extracellular fields and currents — EEG, ECoG, LFP and spikes. *Nature Reviews Neuroscience*. doi:10.1038/nrn3241

[6] Kandel, E. R., Schwartz, J. H., & Jessell, T. M. (2000). *Principles of Neural Science*. *Neurology* (Vol. 4, p. 1414). doi:10.1036/0838577016

[7] Albright, T. D., Kandel, E. R., & Posner, M. I. (2000). Cognitive neuroscience. *Current Opinion in Neurobiology*, *10*, 612–624. doi:10.1016/S0959-4388(00)00132-X

[8] Zhang, J., Laiwalla, F., Kim, J. A., Urabe, H., Van Wagenen, R., Song, Y. K., … Nurmikko, A. V. (2009). A microelectrode array incorporating an optical waveguide device for stimulation and spatiotemporal electrical recording of neural activity. In *Proceedings of the 31st Annual International Conference of the IEEE Engineering in Medicine and Biology Society: Engineering the Future of Biomedicine, EMBC 2009* (pp. 2046–2049). doi:10.1109/IEMBS.2009.5333947

[9] Bradley, J., Luo, R., Otis, T. S., & DiGregorio, D. A. (2009). Submillisecond optical reporting of membrane potential in situ using a neuronal tracer dye. *The Journal of Neuroscience : The Official Journal of the Society for Neuroscience*, *29*, 9197–9209. doi:10.1523/JNEUROSCI.1240-09.2009

[10] Ebner, T. J., & Chen, G. (1995). Use of voltage-sensitive dyes and optical recordings in the central nervous system. *Progress in Neurobiology*, *46*, 463–506. doi:10.1016/0301-0082(95)00010-S

[11] Churchland, P. S., & Sejnowski, T. J. (1988). Perspectives on cognitive neuroscience. *Science (New York, N.Y.)*, *242*, 741–745. doi:10.1126/science.3055294

[12] Cogan, S. F. (2008). Neural stimulation and recording electrodes. *Annual Review of Biomedical Engineering*, *10*, 275–309. doi:10.1146/annurev.bioeng.10.061807.160518

[13] Flemming, K. D. (2006). Essential Neuroscience. *Mayo Clinic Proceedings*. doi:10.4065/81.10.1405-c

[14] Mukamel, R., & Fried, I. (2012). Human Intracranial Recordings and Cognitive Neuroscience. *Annual Review of Psychology*. doi:10.1146/annurev-psych-120709-145401

[15] Blum, R. A., Ross, J. D., Brown, E. A., & DeWeerth, S. P. (2007). An integrated system for simultaneous, multichannel neuronal stimulation and recording. *IEEE Transactions on Circuits and Systems I: Regular Papers, 54*, 2608–2618. doi:10.1109/TCSI.2007.906071

[16] Köhler, P., Eriksson Linsmeier, C., Thelin, J., Bengtsson, M., Jörntell, H., Garwicz, M., … Wallman, L. (2009). Flexible multi electrode brain-machine interface for recording in the cerebellum. In *Proceedings of the 31st Annual International Conference of the IEEE Engineering in Medicine and Biology Society: Engineering the Future of Biomedicine, EMBC 2009* (pp. 536–538). doi:10.1109/IEMBS.2009.5333498

[17] Deisseroth, K. (2011). Optogenetics. *Nature Methods*, *8*, 26–29. doi:10.1038/nmeth.f.324

[18] HajjHassan, M., Chodavarapu, V., & Musallam, S. (2008). NeuroMEMS: Neural probe microtechnologies. *Sensors*. doi:10.3390/s8106704

[19] Glimcher, P. W. (2013). Introduction to Neuroscience. *Neuroeconomics: Decision Making* and the Brain: Second Edition, 63–75. doi:10.1016/B978-0-12-416008-8.00005-X

[20] Grewe, B. F., Voigt, F. F., van ’t Hoff, M., & Helmchen, F. (2011). Fast two-layer two-photon imaging of neuronal cell populations using an electrically tunable lens. Biomedical Optics Express, 2, 2035–2046. doi:10.1364/BOE.2.002035

[21] Viventi, J., Kim, D.-H., Vigeland, L., Frechette, E. S., Blanco, J. A., Kim, Y.-S., … Litt, B. (2011). Flexible, foldable, actively multiplexed, high-density electrode array for mapping brain activity in vivo. *Nature Neuroscience*. doi:10.1038/nn.2973

[22] Akay, M. (2006). *Handbook of Neural Engineering*. *Handbook of Neural Engineering* (pp. 1–662). doi:10.1002/9780470068298

[23] Schjetnan, A. G. P., & Luczak, A. (2011). Recording Large-scale Neuronal Ensembles with Silicon Probes in the Anesthetized Rat. Journal of Visualized Experiments. doi:10.3791/3282

[24] Muthuswamy, J., Okandan, M., Gilletti, A., Baker, M. S., & Jain, T. (2005). An array of microactuated microelectrodes for monitoring single-neuronal activity in rodents. IEEE Transactions on Biomedical Engineering, 52, 1470–1477. doi:10.1109/TBME.2005.851478

[25] Alivisatos, A. P., Andrews, A. M., Boyden, E. S., Chun, M., Church, G. M., Deisseroth, K., … Zhuang, X. (2013). Nanotools for neuroscience and brain activity mapping. *ACS Nano, 7*, 1850–1866. doi:10.1021/nn4012847

[26] Kita, J. M., & Wightman, R. M. (2008). Microelectrodes for studying neurobiology. *Current Opinion in Chemical Biology*. doi:10.1016/j.cbpa.2008.06.035

[27] Musa, S., Welkenhuysen, M., Huys, R., Eberle, W., Van Kuyck, K., Bartic, C., … Borghs, G. (2008). Planar 2D-array neural probe for deep brain stimulation and recording (DBSR). In *IFMBE Proceedings* (Vol. 22, pp. 2421–2425). doi:10.1007/978-3-540-89208-3_581

[28] Rousche, P. J., & Normann, R. A. (1998). Chronic recording capability of the utah intracortical electrode array in cat sensory cortex. *Journal of Neuroscience Methods, 82,* 1–15. doi:10.1016/S0165-0270(98)00031-4

[29] Abbott, L. F. (2008). Theoretical Neuroscience Rising. *Neuron*. doi:10.1016/j.neuron.2008.10.019

[30] Robinson, D. A. (1968). The electrical properties of metal microelectrodes. *Proceedings of the IEEE, 56*. doi:10.1109/PROC.1968.6458

[31] Franks, W., Schenker, I., Schmutz, P., & Hierlemann, A. (2005). Impedance characterization and modeling of electrodes for biomedical applications. *IEEE Transactions on Biomedical* Engineering, 52, 1295–1302. doi:10.1109/TBME.2005.847523

[32] Marin, C., & Fernández, E. (2010). Biocompatibility of intracortical microelectrodes: current status and future prospects. Frontiers in Neuroengineering, 3, 8. doi:10.3389/fneng.2010.00008

[33] Kim, J.-H., Kang, G., Nam, Y., & Choi, Y.-K. (2010). Surface-modified microelectrode array with flake nanostructure for neural recording and stimulation. *Nanotechnology*, *21*, 85303. doi:10.1088/0957-4484/21/8/085303

[34] Kimling, J., Maier, M., Okenve, B., Kotaidis, V., Ballot, H., & Plech, A. (2006). Turkevich method for gold nanoparticle synthesis revisited. *Journal of Physical Chemistry B*, *110*, 15700–15707. doi:10.1021/jp061667w

[35] Santos, L., Neto, J. P., Crespo, A., Nunes, D., Costa, N., Fonseca, I. M., … Fortunato, E. (2014). WO3 Nanoparticle-Based Conformable pH Sensor. *ACS Applied Materials & Interfaces*. doi:10.1021/am501724h

[36] Shi, Y. (2013). Optimization Conditions for Single-Walled Carbon Nanotubes Dispersion. *Journal of Surface Engineered Materials and Advanced Technology, 03,* 6–12. doi:10.4236/jsemat.2013.31002

[37] Atlas, A. M. B. (2009). Allen Brain Atlas. Retrieved from hhtp://mouse.brain-map.org

[38] Dias, N. S., Silva, M. F., Ribeiro, J. F., Cardoso, V. F., Jacinto, L. R., Oliveira, J. F., … Correia, J. H. (2011). Gold coated SU-8-based microelectrodes for in vivo electrophysiological studies: Rapid prototyping protocol-specific microelectrode designs. In *2011 5th International IEEE/EMBS Conference on Neural Engineering, NER 2011* (pp. 310–313). doi:10.1109/NER.2011.5910549

[39] Leyva-Pérez, A., Doménech, A., Al-Resayes, S. I., & Corma, A. (2012). Gold redox catalytic cycles for the oxidative coupling of alkynes. *ACS Catalysis*, *2,* 121–126. doi:10.1021/cs200532c

[40] Mansfeld, F. (1990). Electrochemical impedance spectroscopy (EIS) as a new tool for investigating methods of corrosion protection. *Electrochimica Acta*. doi:10.1016/0013-4686(90)80007-B

[41] Cao, G., Liu, Q., Huang, Y., Li, W., & Yao, S. (2010). Generation of gold nanostructures at the surface of platinum electrode by electrodeposition for ECL detection for CE. *Electrophoresis*, *31*, 1055–1062. doi:10.1002/elps.200900433

[42] Wang, J., Yang, Z., Wang, X., & Yang, N. (2008). Capillary electrophoresis with gold nanoparticles enhanced electrochemiluminescence for the detection of roxithromycin. *Talanta*, *76*, 85–90. doi:10.1016/j.talanta.2008.02.006

[43] Kim, K. H., Kim, J. U., Cha, S. H., & Lee, J. C. (2009). Reversible formation and dissolution of gold nanoparticles through turning on and off sequences of UV light. *Journal of the American Chemical Society*, *131*, 7482–7483. doi:10.1021/ja8088394

[44] Carrillo, J. M. Y., Raphael, E., & Dobrynin, A. V. (2010). Adhesion of nanoparticles. *Langmuir*, *26*, 12973–12979. doi:10.1021/la101977c

[45] Cui, X., & Martin, D. C. (2003). Electrochemical deposition and characterization of poly(3,4-ethylenedioxythiophene) on neural microelectrode arrays. *Sensors and Actuators, B: Chemical*, *89*, 92–102. doi:10.1016/S0925-4005(02)00448-3

[46] Chen, S., Zhao, Z., & Liu, H. (2013). Charge transport at the metal-organic interface. Annual Review of Physical Chemistry, 64, 221–45. doi:10.1146/annurev-physchem-040412-110035

[47] Gerwig, R., Fuchsberger, K., Schroeppel, B., Link, G. S., Heusel, G., Kraushaar, U., … Stelzle, M. (2012). PEDOT–CNT Composite Microelectrodes for Recording and Electrostimulation Applications: Fabrication, Morphology, and Electrical Properties. *Frontiers in Neuroengineering*. doi:10.3389/fneng.2012.00008

[48] Zou, B. X., Liang, Y., Liu, X. X., Diamond, D., & Lau, K. T. (2011). Electrodeposition and pseudocapacitive properties of tungsten oxide/polyaniline composite. *Journal of Power Sources*, *196*, 4842–4848. doi:10.1016/j.jpowsour.2011.01.073

[49] Lempka, S. F. (2010). THE ELECTRODE-TISSUE INTERFACE DURING RECORDING AND STIMULATION IN THE CENTRAL NERVOUS SYSTEM. *Thesis*.

[50] Lasia, A. (1999). Electrochemical Impedance Spectroscopy and its Applications. *Modern Aspects Of Electrochemistry*, *32*, 143–248. doi:10.1007/0-306-46916-2_2

[51] Chang, B.-Y., & Park, S.-M. (2010). Electrochemical impedance spectroscopy. *Annual Review of Analytical Chemistry (Palo Alto, Calif.)*, *3*, 207–229. doi:10.1146/annurev.anchem.012809.102211

[52] Cui, X., & Martin, D. C. (2003). Fuzzy gold electrodes for lowering impedance and improving adhesion with electrodeposited conducting polymer films. *Sensors and Actuators, A: Physical*, *103*, 384–394. doi:10.1016/S0924-4247(02)00427-2

6. Appendix

Section A

Silicon probes with different configuration used on this work, obtained by optical microscopy.

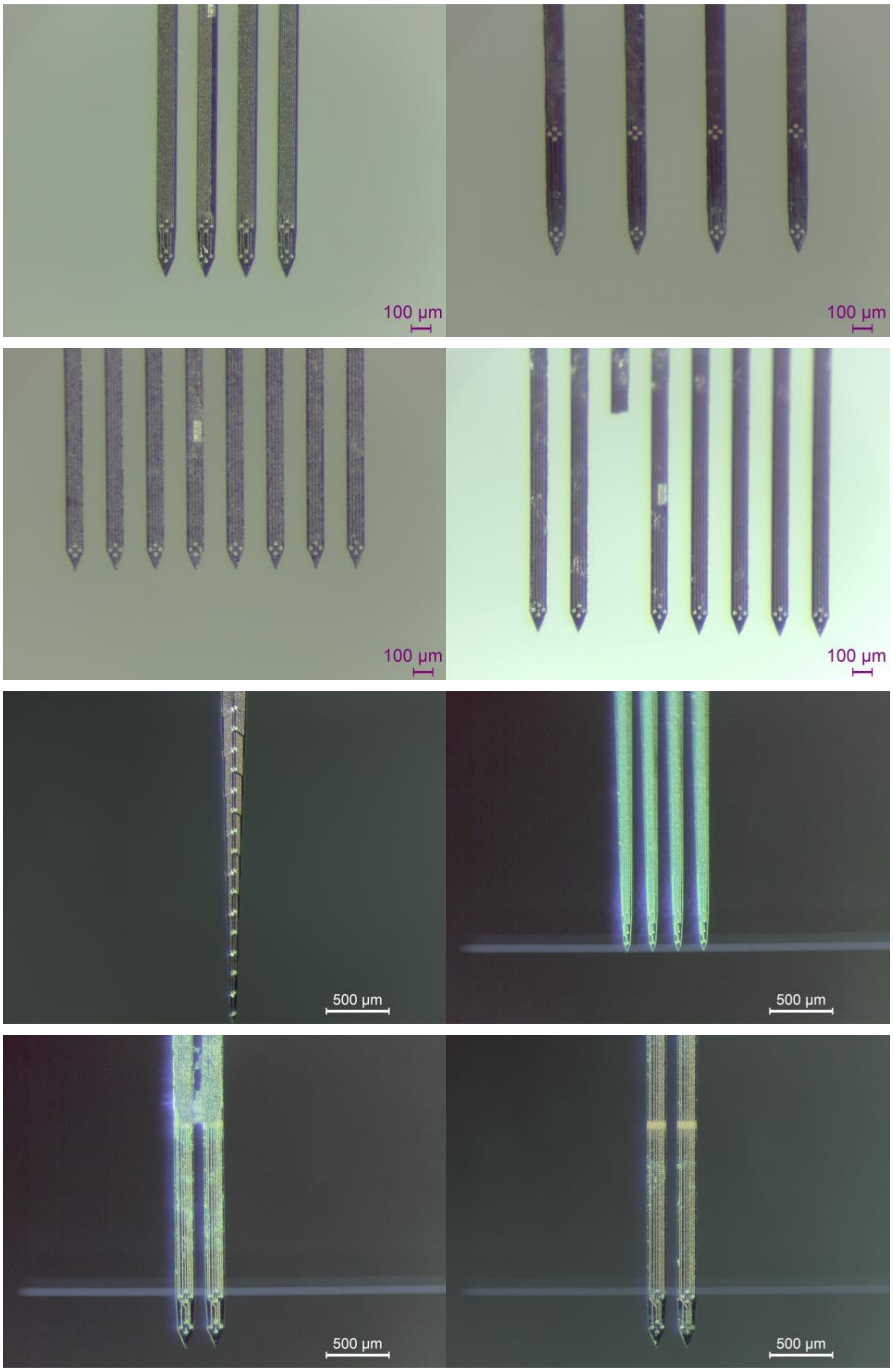

Figure 6.1 – Optical microscope images taken for multiple silicon probe configurations used during this work.

Section B

Python scripts used for data analysis of acute neural recordings:

Script #1

```
import os
import numpy as np
import scipy.signal as signal
import matplotlib.pyplot as plt
import trigger_probes as trig

### DATA PROCESSING ###
def align_data(data,indices,before=0,after=0):
    columns = np.shape(data)[1]
    return [data[:,slice(index-before,index+after+1)] for index in indices if index-before >= 0 and index+after < columns]

def find_peaks(data,threshold,minstep=0):
    derivative = np.diff(np.sign(np.diff(data)))
        if threshold > 0:
            derivative = derivative < 0
        else:
            derivative = derivative > 0
        peaks = derivative.nonzero()[0] + 1 # local max
        if threshold > 0:
            peaks = peaks[data[peaks] > threshold]
        else:
            peaks = peaks[data[peaks] < threshold]
        if minstep > 0:
            gpeaks = split_list_pairwise(peaks,lambda x,p:x-p > minstep)
            peaks = np.array([g[np.argmax([data[i] for i in g])] for g in gpeaks])
        return peaks

def loadRawData(filename,numChannels,dtype):
    fdata = np.fromfile(filename,dtype=dtype)
    numsamples = len(fdata) / numChannels
    data = np.reshape(fdata,(numsamples,numChannels))
    return (np.transpose(data))

def highpass(data,sampleFreq=30000.0,passFreq=500.0,stopFreq=100.0):
    # Define High Pass-band
    wp = passFreq/sampleFreq
```

```
    ws = stopFreq/sampleFreq
    # Filter Data with Butterworth (HighPass)
    N, wn = signal.buttord(wp, ws, 3, 16) # (?)
    b, a = signal.butter(N, wn, btype='high')
   return signal.lfilter(b,a,data)
```

Script #2

```
import os
import numpy as np
import scipy.signal as signal
import numpy as np
import matplotlib as mpl
import matplotlib.pyplot as plt
import trigger_probes as trig
from scipy import stats


def extra_trigger_analysis(filename,triggerchannel=18,threshold=-80,minstep=100,before=500,after=500):
    global amplifier, filtamplifier, triggers, alignamplifier
    amplifier = trig.loadRawData(filename,numChannels=32,dtype=np.float32)
    filtamplifier = np.float32(trig.highpass(amplifier[:,:],passFreq=500.0,stopFreq=300.0))
    trigchannel = filtamplifier[triggerchannel,:]
    triggers = trig.find_peaks(trigchannel,threshold,minstep) # Trigger on spikes
    alignamplifier = np.dstack(trig.align_data(filtamplifier,triggers,before,after))

### PLOTTING ####

def triggerline(x):
    if x is not None:
    ylim = plt.ylim()
    plt.vlines(x,ylim[0],ylim[1])

def plot_triggers(triggerdata,channeloffset=0,trigger=None,**kwargs):
    number_samples=np.shape(triggerdata)[1]
    time_sec=number_samples/30000.0
    resolucao= time_sec/number_samples
    x_adc=np.arange(0, time_sec, resolucao)
    for t in range(np.shape(triggerdata)[2]):
        data = triggerdata[:,:,t]
```

```
        rows = np.shape(data)[0]
        offset = np.arange(rows) * channeloffset
        plt.plot(x_adc, data.T + offset,**kwargs) ##### mV andf msec
        triggerline(trigger)

def plot_triggers_single_channel(triggerdata,channel,trigger=None,number_widows=1,**kwargs):
    number_samples=np.shape(triggerdata)[1]
    time_sec=number_samples/30000.0
    resolucao= time_sec/number_samples
    x_adc=np.arange(0, time_sec*1000.0, resolucao*1000.0)
    for t in range(np.shape(triggerdata)[2]):
        data = triggerdata[channel,:,t]
        plt.plot( x_adc,data,**kwargs) ##### mV andf msec
        triggerline(trigger)
        v = [15,19,-310,250]
        axis(v)

def plot_trigger_average(triggerdata,channeloffset=0,trigger=None,**kwargs):
    global data
    global x_adc

    data = np.mean(alignamplifier[channel,:,:], axis = 1)
    number_samples=np.shape(alignamplifier)[1]
    time_sec=number_samples/30000.0
    resolucao= time_sec/number_samples
    x_adc=np.arange(0, time_sec*1000.0, resolucao*1000.0)
    plt.plot(x_adc,data,'black')
    amplitude = abs(min(data))+abs(max(data))
    stdv = np.mean(std(alignamplifier[channel,:,:],axis=1))
    negative_error= (np.mean(alignamplifier[channel,:,:],axis=1)-(stdv))
    positive_error= (np.mean(alignamplifier[channel,:,:], axis=1)+(stdv))
    plt.fill_between(x_adc,negative_error,positive_error,alpha=0.2)
    SNR = (max(data)-min(data))/(2*stdv)
    print SNR
    print amplitude
    print stdv
    v = [15,19,-310,250]
    axis(v)
    triggerline(500/30)
```

```
    resolucao= time_sec/number_samples
    x_adc=np.arange(0, time_sec*1000.0, resolucao*1000.0)
    plt.plot(x_adc, data.T + offset,**kwargs)
    triggerline(trigger)

####NEURONEXUS sites geometry

def plot_trigger_average_mapp_visualization(triggerdata,yaxis=80,trigger=None,**kwargs):
    global data
    global x_adc
    number_samples=np.shape(triggerdata)[1]
    time_sec=number_samples/30000.0
    resolucao= time_sec/number_samples
    x_adc=np.arange(0, time_sec*1000.0, resolucao*1000.0)
    stdv= stats.sem(triggerdata, axis=2)
    negative_error= (np.mean(triggerdata,axis=2)-(stdv))
    positive_error= (np.mean(triggerdata,axis=2)+(stdv))
    subplot(22,3,2)#channel 0
    plt.plot(x_adc, data[0,:].T)
    plt.fill_between(x_adc,negative_error[0,:],positive_error[0,:], alpha=0.2,facecolor='#FF9848')
    ylim((-yaxis,yaxis))
    xlim((15.5,18.5))
    subplot(22,3,5)#channel 31
    plt.plot(x_adc, data[31,:].T)
    plt.fill_between(x_adc,negative_error[31,:],positive_error[31,:], alpha=0.2,facecolor='#FF9848')
    ylim((-yaxis,yaxis))
    xlim((15.5,18.5))

    subplot(22,3,7)#channel 24
    plt.fill_between(x_adc,negative_error[24,:],positive_error[24,:], alpha=0.2,facecolor='#FF9848')
    plt.plot(x_adc, data[24,:].T)
    ylim((-yaxis,yaxis))
    xlim((15.5,18.5))

    subplot(22,3,9)#channel7
    plt.plot(x_adc, data[7,:].T)
```

```
    plt.fill_between(x_adc,negative_error[7,:],positive_error[7,:], alpha=0.2,face-
color='#FF9848')
    ylim((-yaxis,yaxis))
    xlim((15.5,18.5))
    subplot(22,3,11)#1
    plt.plot(x_adc, data[1,:].T)
    plt.fill_between(x_adc,negative_error[1,:],positive_error[1,:], alpha=0.2,face-
color='#FF9848')
    ylim((-yaxis,yaxis))
    xlim((15.5,18.5))
    subplot(22,3,13)#channel21
    plt.plot(x_adc, data[21,:].T)
    plt.fill_between(x_adc,negative_error[21,:],positive_error[21,:], alpha=0.2,face-
color='#FF9848')
    ylim((-yaxis,yaxis))
    xlim((15.5,18.5))
    subplot(22,3,15)#channel10
    plt.plot(x_adc, data[10,:].T)
    plt.fill_between(x_adc,negative_error[10,:],positive_error[10,:], alpha=0.2,face-
color='#FF9848')
    ylim((-yaxis,yaxis))
    xlim((15.5,18.5))
    subplot(22,3,17)#channel30
    plt.plot(x_adc, data[30,:].T)
    plt.fill_between(x_adc,negative_error[30,:],positive_error[30,:], alpha=0.2,face-
color='#FF9848')
    ylim((-yaxis,yaxis))
    xlim((15.5,18.5))
    subplot(22,3,19)#channel25
    plt.plot(x_adc, data[25,:].T)
    plt.fill_between(x_adc,negative_error[25,:],positive_error[25,:], alpha=0.2,face-
color='#FF9848')
    ylim((-yaxis,yaxis))
    xlim((15.5,18.5))
    subplot(22,3,21)#channel6
    plt.plot(x_adc, data[6,:].T)
    plt.fill_between(x_adc,negative_error[6,:],positive_error[6,:], alpha=0.2,face-
color='#FF9848')
    ylim((-yaxis,yaxis))
    xlim((15.5,18.5))
```

```
subplot(22,3,23)#channel15
plt.plot(x_adc, data[15,:].T)
plt.fill_between(x_adc,negative_error[15,:],positive_error[15,:], alpha=0.2,facecolor='#FF9848')
ylim((-yaxis,yaxis))
xlim((15.5,18.5))
subplot(22,3,25)#channel20
plt.plot(x_adc, data[20,:].T)
plt.fill_between(x_adc,negative_error[20,:],positive_error[20,:], alpha=0.2,facecolor='#FF9848')
ylim((-yaxis,yaxis))
xlim((15.5,18.5))
subplot(22,3,27)#channel11
plt.plot(x_adc, data[11,:].T)
plt.fill_between(x_adc,negative_error[6,:],positive_error[6,:], alpha=0.2,facecolor='#FF9848')
ylim((-yaxis,yaxis))
xlim((15.5,18.5))
subplot(22,3,29)#channel16
plt.plot(x_adc, data[16,:].T)
plt.fill_between(x_adc,negative_error[16,:],positive_error[16,:], alpha=0.2,facecolor='#FF9848')
ylim((-yaxis,yaxis))
xlim((15.5,18.5))
subplot(22,3,31)#channel26
plt.plot(x_adc, data[26,:].T)
plt.fill_between(x_adc,negative_error[26,:],positive_error[26,:], alpha=0.2,facecolor='#FF9848')
ylim((-yaxis,yaxis))
xlim((15.5,18.5))
subplot(22,3,33)#channel5
plt.plot(x_adc, data[5,:].T)
plt.fill_between(x_adc,negative_error[5,:],positive_error[5,:], alpha=0.2,facecolor='#FF9848')
ylim((-yaxis,yaxis))
xlim((15.5,18.5))
subplot(22,3,35)#channel14
plt.plot(x_adc, data[14,:].T)
plt.fill_between(x_adc,negative_error[14,:],positive_error[14,:], alpha=0.2,facecolor='#FF9848')
```

```
ylim((-yaxis,yaxis))
xlim((15.5,18.5))
subplot(22,3,37)#channel19
plt.plot(x_adc, data[19,:].T)
plt.fill_between(x_adc,negative_error[19,:],positive_error[19,:], alpha=0.2,facecolor='#FF9848')
ylim((-yaxis,yaxis))
xlim((15.5,18.5))
subplot(22,3,39)#channel12
plt.plot(x_adc, data[12,:].T)
plt.fill_between(x_adc,negative_error[12,:],positive_error[12,:], alpha=0.2,facecolor='#FF9848')
ylim((-yaxis,yaxis))
xlim((15.5,18.5))
subplot(22,3,41)#channel17
plt.plot(x_adc, data[17,:].T)
plt.fill_between(x_adc,negative_error[17,:],positive_error[17,:], alpha=0.2,facecolor='#FF9848')
ylim((-yaxis,yaxis))
xlim((15.5,18.5))
subplot(22,3,43)#channel27
plt.plot(x_adc, data[27,:].T)
plt.fill_between(x_adc,negative_error[27,:],positive_error[27,:], alpha=0.2,facecolor='#FF9848')
ylim((-yaxis,yaxis))
xlim((15.5,18.5))
subplot(22,3,45)#channel4
plt.plot(x_adc, data[4,:].T)
plt.fill_between(x_adc,negative_error[4,:],positive_error[4,:], alpha=0.2,facecolor='#FF9848')
ylim((-yaxis,yaxis))
xlim((15.5,18.5))
subplot(22,3,47)#channel8
plt.plot(x_adc, data[8,:].T)
plt.fill_between(x_adc,negative_error[8,:],positive_error[8,:], alpha=0.2,facecolor='#FF9848')
ylim((-yaxis,yaxis))
xlim((15.5,18.5))
subplot(22,3,49)#channel18
plt.plot(x_adc, data[18,:].T)
```

```
    plt.fill_between(x_adc,negative_error[18,:],positive_error[18,:], alpha=0.2,facecolor='#FF9848')
    ylim((-yaxis,yaxis))
    xlim((15.5,18.5))
    subplot(22,3,51)#channel13
    plt.plot(x_adc, data[13,:].T)
    plt.fill_between(x_adc,negative_error[13,:],positive_error[13,:], alpha=0.2,facecolor='#FF9848')
    ylim((-yaxis,yaxis))
    xlim((15.5,18.5))
    subplot(22,3,53)#channel23
    plt.plot(x_adc, data[23,:].T)
    plt.fill_between(x_adc,negative_error[23,:],positive_error[23,:], alpha=0.2,facecolor='#FF9848')
    ylim((-yaxis,yaxis))
    xlim((15.5,18.5))
    subplot(22,3,55)#channel28
    plt.plot(x_adc, data[28,:].T)
    plt.fill_between(x_adc,negative_error[28,:],positive_error[28,:], alpha=0.2,facecolor='#FF9848')
    ylim((-yaxis,yaxis))
    xlim((15.5,18.5))
    subplot(22,3,57)#channel3
    plt.plot(x_adc, data[3,:].T)
    plt.fill_between(x_adc,negative_error[3,:],positive_error[3,:], alpha=0.2,facecolor='#FF9848')
    ylim((-yaxis,yaxis))
    xlim((15.5,18.5))
    subplot(22,3,59)#channel9
    plt.plot(x_adc, data[9,:].T)
    plt.fill_between(x_adc,negative_error[9,:],positive_error[9,:], alpha=0.2,facecolor='#FF9848')
    ylim((-yaxis,yaxis))
    xlim((15.5,18.5))
    subplot(22,3,61)#channel29
    plt.plot(x_adc, data[29,:].T)
    plt.fill_between(x_adc,negative_error[29,:],positive_error[29,:], alpha=0.2,facecolor='#FF9848')
    ylim((-yaxis,yaxis))
    xlim((15.5,18.5))
```

```
subplot(22,3,63)#channel2
plt.plot(x_adc, data[2,:].T)
plt.fill_between(x_adc,negative_error[2,:],positive_error[2,:], alpha=0.2,facecolor='#FF9848')
ylim((-yaxis,yaxis))
xlim((15.5,18.5))
subplot(22,3,65)#channel22
plt.plot(x_adc, data[22,:].T)
plt.fill_between(x_adc,negative_error[22,:],positive_error[22,:], alpha=0.2,facecolor='#FF9848')
ylim((-yaxis,yaxis))
xlim((15.5,18.5))
```

Section C

Impedance and charge storage capacity values obtained for the different coatings used.

C.1. Commercial gold solution

Table 6.1 - Impedance values and charge storage capacity obtained for gold depositions with different coating times.

Coating Time (s)	Initial Z (kΩ)	Z after coating (kΩ)	Z_{drop} (%)	C_{sc} (nF)
Pristine	1032.5±1.2	-	-	2.67
90	1114.7±2.5	687.0±5.3	38.4	-
120	923.7±14.9	220.7±2.5	76.1	9.4
180	951.7±7.2	52.7±0.6	94.5	11.74

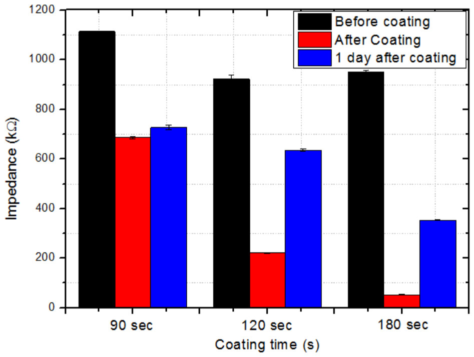

Figure 6.2 - Impedance drop after deposition for different coating times and stability after one day given by impedance rising.

C.2. Gold nanoflakes solution

Table 6.2 – Impedance values and charge storage capacity obtained for gold nanoflakes depositions with different coating times.

Coating Time (s)	Initial Z (kΩ)	Z after coating (kΩ)	Z_{drop} (%)	C_{sc} (nF)
Pristine	1032.5±1.2	-	-	2.67
30	1208.3±3.2	230.3 ±1.2	81	6.2
120	1740.7±10.1	343±2.4	80.3	34.4
180	1004±10.1	517.3±4.2	48	23.5

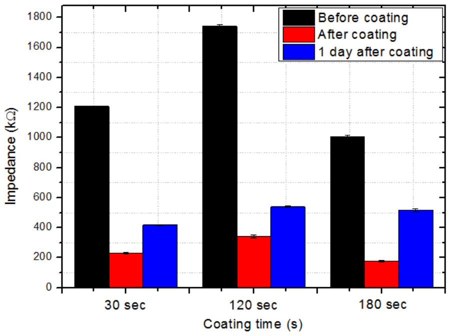

Figure 6.3 - Impedance drop after deposition for different coating times and stability after one day given by impedance rising.

C.3. Gold nanoparticles (Au NPs)

Table 6.3 – Impedance values (at 1004 Hz) and charge storage capacity obtained for gold depositions with different coating times.

Coating	Initial Z (kΩ)	Z after coating (kΩ)	Z_{drop} (%)	C_{sc} (nF)
Pristine	967±5.1	-	-	3.18
AuNPs	1060±2.0	648.3±10.1	38.8	7.01

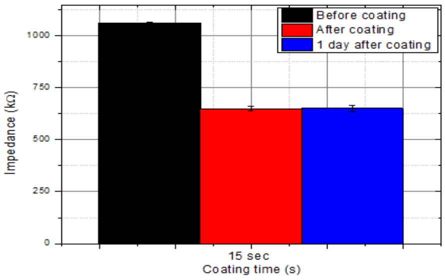

Figure 6.4 - Impedance drop after deposition for different coating times and stability after one day given by impedance rising.

C.4. PEDOT:PSS

Table 6.4 – Impedance values (at 1004 Hz) and charge storage capacity obtained for gold depositions with different coating times.

Coating Time (s)	Initial Z (kΩ)	Z after coating (kΩ)	Z_{drop} (%)	C_{sc} (nF)
Pristine	1032.5±1.2	-	-	2.67
5	1054.33	35	96.7	22.67
15	1053.71	25	97.6	44.1

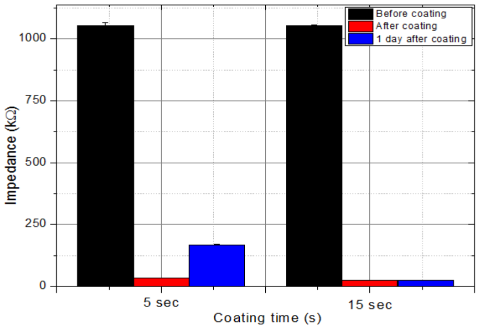

Figure 6.5 - Impedance drop after deposition for different coating times and stability after one day given by impedance rising.

C.5. PEDOT:AuNPs

Table 6.5 - Impedance values (at 1004 Hz) and charge storage capacity obtained for gold depositions with different coating times.

PEDOT:AuNPs Ratio	Initial Z (kΩ)	Z after coating (kΩ)	Z_{drop} (%)	C_{sc} (nF)
Pristine	1032.5±1.2	-	-	2.67
4:05	975.1±3.4	25.3±0.3	97.4	101.71

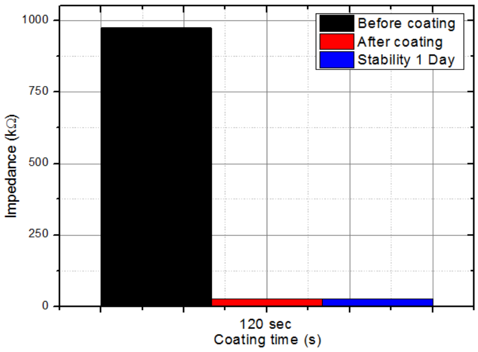

Figure 6.6 - Impedance drop after deposition for different coating times and stability after one day given by impedance rising.

C.6. PEDOT:CNTs

Table 6.6 - Impedance values (at 1004 Hz) and charge storage capacity obtained for gold depositions with different coating times.

PEDOT:CNT Ratio	Initial Z (kΩ)	Z after coating (kΩ)	Z_{drop} (%)	C_{sc} (nF)
Pristine	1032.5±1.2	-	-	2.67
4:1	891.7±4.1	35.3±0.6	96	75.3
4:3.5	994.7±2.1	92.7	90.7	55.7

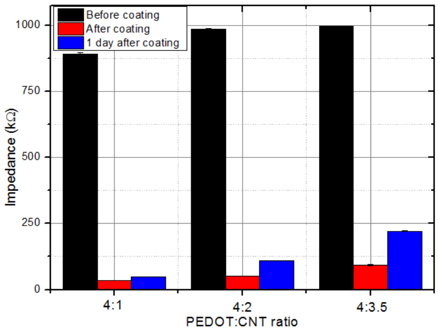

Figure 6.7 - Impedance drop for PEDOT:CNT modifications after deposition for different coating concentrations and stability after one day (given by impedance rising).

C.7. Tungsten Oxide Nanoparticles

Table 6.7 - Impedance values (at 1004 Hz) and charge storage capacity obtained for gold depositions with different coating times.

Coating	Initial Z (kΩ)	Z after coating (kΩ)	Z_{drop} (%)	C_{sc} (nF)
Pristine	638±3.2	-	-	7.2
WO_3	613.1±2.5	374±3.4	39	8.1

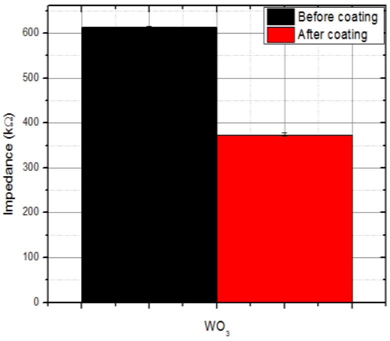

Figure 6.8 - Impedance drop for WO_3 modifications after deposition for different coating concentrations and stability after one day (given by impedance rising). No data for 1 day after deposition is shown the impedance return to its original values.

Section D

Summary of all the important results obtained throughout this work.

Table 6.8 – Best results obtained for differing electrode coatings.

Coating	Current (nA)	Time (s)	$\lvert Z_{drop} \rvert$(%)	C_{sc} (mC/cm^2)
Pristine	-	-	-	2.2
Commercial Gold	-30	120	76.1	5.3
Au-PVP	-30	120	80.3	19.5
Au NPs	-	-	-	-
PEDOT	+30	5	96.7	36.4
PEDOT-AuNPs	+30	30	97.4	84.1
PEDOT-CNTs	+30	30	96	62.2
WO3 NPs	-	-	-	-

Section E

Electrical component values obtained for the electronic scheme of the electrodes.

Table 6.9 - List of elements, corresponding symbols and relations of admittance and impedance.

Element description	Symbol	Admitance	Impedance	Parameters
Resistance	R	1/R	R	R
Capacitance	C	jωC	-j/ωC	C
Inductance	L	-j/ωL	jωL	L
Warburg	W	$Y_0\sqrt{(j\omega)}$	$1/Y_0\sqrt{(j\omega)}$	Y_0
CPE	Q	$Y_0(j\omega)^n$	$(j\omega)^{-n}/Y_0$	Y_0, n

The equation that models the impedance of this system is composed by different electrical components is given by:

$$Z_T = Z_1 + \frac{Z_4(Z_2 + Z_3)}{Z_2 + Z_3 + Z_4} + \frac{Z_5 Z_6}{Z_5 + Z_6} \quad \textbf{Eq. 4.1}$$

$$Z_1 = R_E \quad \textbf{Eq. 4.2}$$

$$Z_2 = R_p \quad \textbf{Eq. 4.3}$$

$$Z_3 = \frac{R_{CT1}(j\omega)^{-n}/Y_{0CPE2}}{R_{CT1} + (j\omega)^{-n}/Y_{0CPE2}} \quad \textbf{Eq. 4.4}$$

$$Z_4 = \frac{(j\omega)^{-n}}{Y_{0CPE1}} \quad \textbf{Eq. 4.5}$$

$$Z_5 = \frac{(j\omega)^{-n}}{Y_{0CPE3}} \quad \textbf{Eq. 4.6}$$

$$Z_6 = R_{CT2} + \frac{1}{Y_0\sqrt{j\omega}} \quad \textbf{Eq. 4.7}$$

Equivalent Circuit fitting parameters

Pristine Electrode

Table 6.10 - Equivalent circuit parameters calculated via Gamry Echem Analyst Software for fitting the data from a pristine electrode.

Parameter	Value	Error	Unit
R_E	22.34 x 10^{-3}	1.972 x 10^{3}	Ω
R_P	32.31 x 10^{3}	11.22 x 10^{3}	Ω
R_{CT1}	1.163 x 10^{3}	564.2 x 10^{3}	Ω
R_{CT2}	713.4 x 10^{3}	7.190 x 10^{9}	Ω
CPE_1	19.74 x 10^{-12}	28.64 x 10^{-12}	$S.s^n$
CPE_2	2.45 x 10^{-9}	1.56 x 10^{-9}	$S.s^n$
CPE_3	238.0 x 10^{-12}	453.9 x 10^{-12}	$S.s^n$
n_1	0.953	0.110	
n_2	0.778	0.077	
n_3	0.948	0.142	
W	259.9 x 10^{-12}	64.32 x10^{-12}	$S.s^{1/2}$
Goodness of Fit	287.3 x 10^{-6}	-	

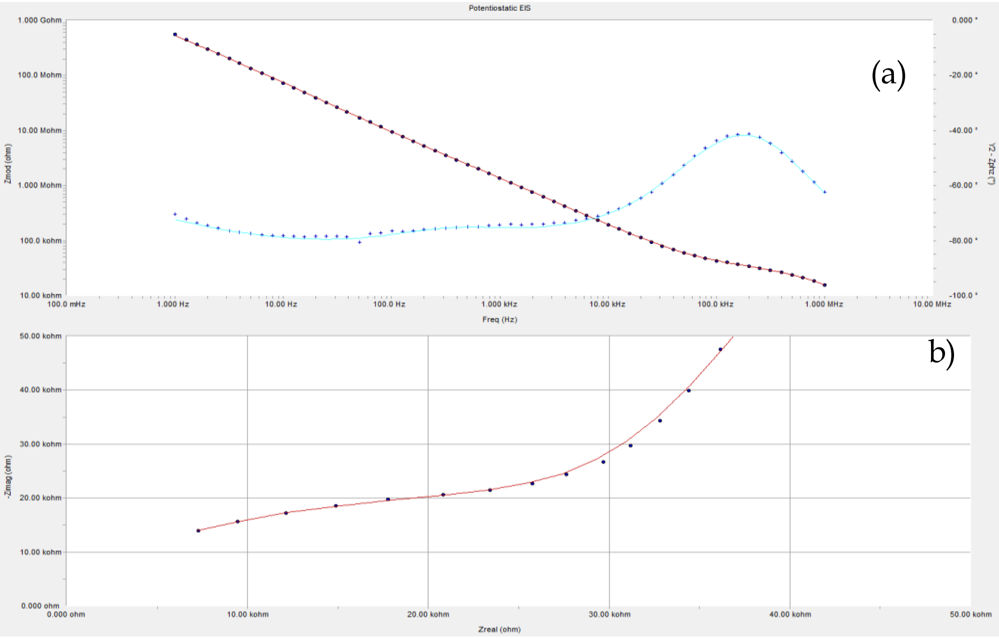

Figure 6.9 - Electrochemical Impedance Spectroscopy spectra given by Gamry Echem Analyst Software. Bode plot on (a) and niquist plot on (b) for a pristine electrode with the respective data fitting.

Commercial gold electrode

Table 6.11 - Equivalent circuit parameters calculated via Gamry Echem Analyst Software for fitting the data from an electrode modified with a commercial gold solution.

Parameter	Value	Error	Unit
R_E	66.24×10^{-6}	1.489×10^{3}	Ω
R_P	37.26×10^{3}	7.967×10^{3}	Ω
R_{CT1}	3.59×10^{6}	50.06×10^{6}	Ω
R_{CT2}	95.26×10^{6}	883.1×10^{6}	Ω
CPE_1	29.12×10^{-12}	26.36×10^{-12}	$S.s^n$
CPE_2	34.00×10^{-9}	234.6×10^{-9}	$S.s^n$
CPE_3	1.21×10^{-9}	3.32×10^{-9}	$S.s^n$
n_1	0.929	0.065	
n_2	0.649	0.463	
n_3	0.993	0.503	
W	2.18×10^{-9}	497.7×10^{-12}	$S.s^{1/2}$
Goodness of Fit	95.88×10^{-6}	-	

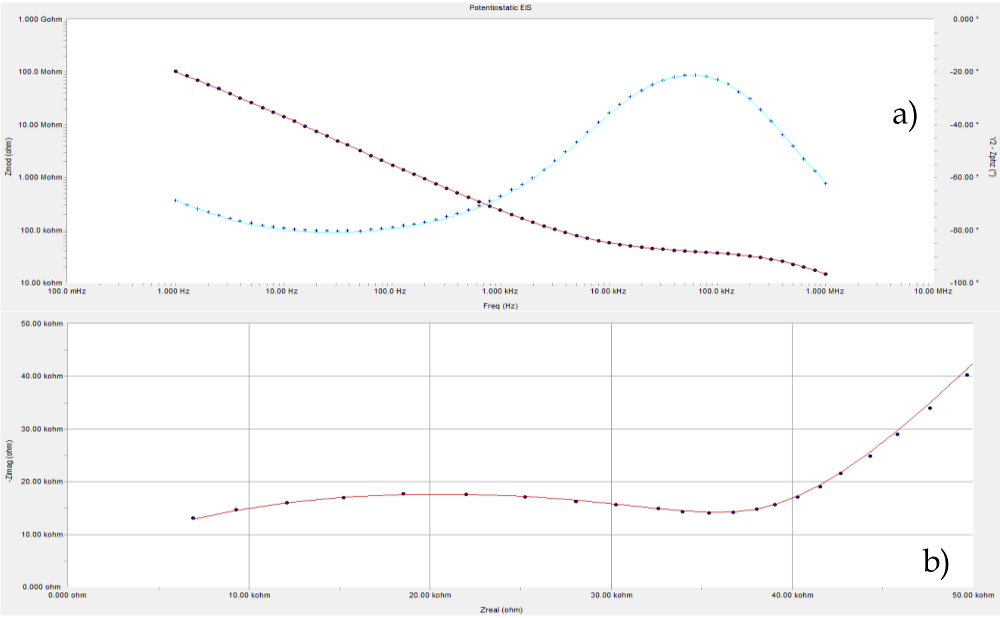

Figure 6.10 - Electrochemical Impedance Spectroscopy spectra given by Gamry Echem Analyst Software. Bode plot on (a) and niquist plot on (b) for a commercial gold solution coating with the respective data fitting.

Gold Nanoparticles electrode

Table 6.12 - Equivalent circuit parameters calculated via Gamry Echem Analyst Software for fitting the data from an electrode modified with gold nanoparticles.

Parameter	Value	Error	Unit
R_E	4.444	1.951×10^{3}	Ω
R_P	25.10×10^{3}	3.391×10^{3}	Ω
R_{CT1}	180.6×10^{3}	153.1×10^{3}	Ω
R_{CT2}	998.7×10^{6}	313.2×10^{6}	Ω
CPE_1	28.04×10^{-12}	32.91×10^{-12}	$S.s^n$
CPE_2	23.59×10^{-9}	16.99×10^{-9}	$S.s^n$
CPE_3	731.8×10^{-12}	39.37×10^{-12}	$S.s^n$
n_1	0.931	0.085	
n_2	0.693	0.073	
n_3	0.906	0.011	
W	4.237×10^{-3}	13.75×10^{3}	$S.s^{1/2}$
Goodness of Fit	282.3×10^{-6}	-	

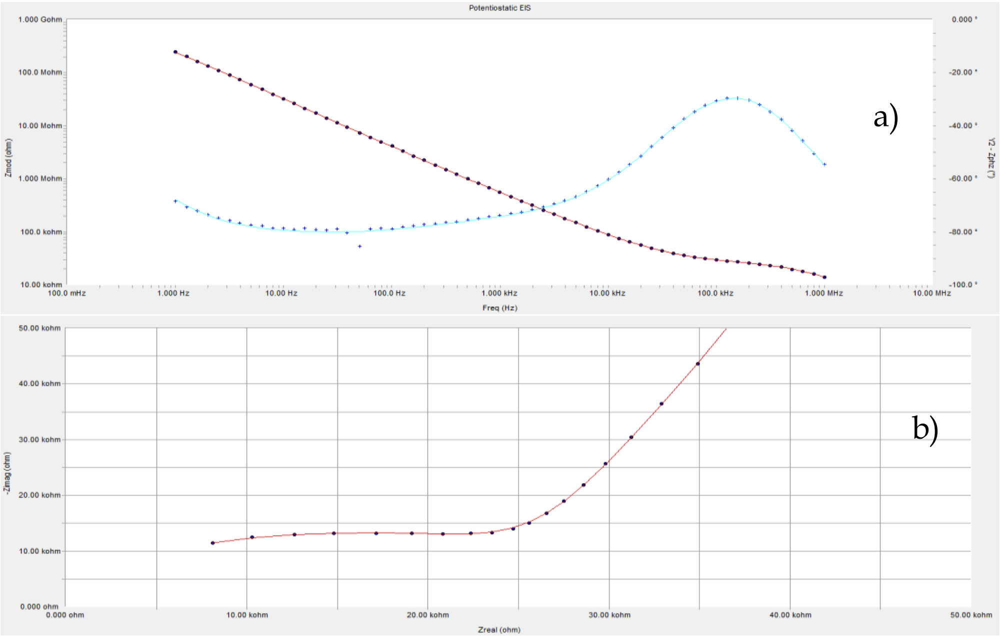

Figure 6.11 - Electrochemical Impedance Spectroscopy spectra given by Gamry Echem Analyst Software. Bode plot on (a) and niquist plot on (b) for gold nanoparticles coating with the respective data fitting.

PEDOT:PSS

Table 6.13 - Equivalent circuit parameters calculated via Gamry Echem Analyst Software for fitting the data from an electrode modified with PEDOT:PSS.

Parameter	Value	Error	Unit
R_E	472.6	$2.929x10^3$	Ω
R_P	$22.91x10^3$	$4.937x10^3$	Ω
R_{CT1}	$4.44x10^3$	$6.75x10^3$	Ω
R_{CT2}	$334.8x10^3$	$123.3x10^9$	Ω
CPE_1	$13.35x10^{-12}$	$22.28x10^{-12}$	$S.s^n$
CPE_2	$112.3x10^{-9}$	$599.2x10^{-9}$	$S.s^n$
CPE_3	$8.22x10^{-9}$	$53.43x10^{-9}$	$S.s^n$
n_1	0.965	0.122	
n_2	0.675	0.567	
n_3	0.991	0.053	
W	$655.0x10^{-12}$	$1.289x10^{-9}$	$S.s^{1/2}$
Goodness of Fit	$9.858x10^{-6}$	-	

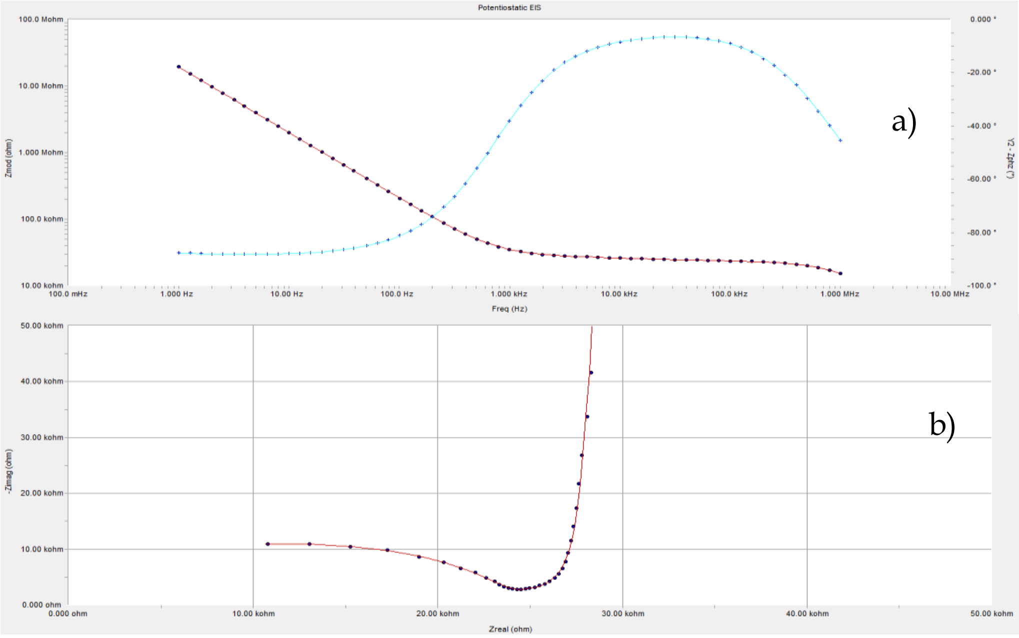

Figure 6.12 - Electrochemical Impedance Spectroscopy spectra given by Gamry Echem Analyst Software. Bode plot on (a) and niquist plot on (b) for a PEDOT coating with the respective data fitting.

Gold Nanoflakes

Table 6.14 - Equivalent circuit parameters calculated via Gamry Echem Analyst Software for fitting the data from an electrode modified with gold nanoflakes.

Parameter	Value	Error	Unit
R_E	32.95	$2.575x10^3$	Ω
R_P	$26.05x10^3$	$7.352x10^3$	Ω
R_{CT1}	$184.6x10^3$	$164.0x10^3$	Ω
R_{CT2}	$964.9.8x10^3$	$430.5x10^6$	Ω
CPE_1	$13.32x10^{-12}$	$38.07x10^{-12}$	$S.s^n$
CPE_2	$112.3x10^{-9}$	$599.2x10^{-9}$	$S.s^n$
CPE_3	$4.973x10^{-9}$	$3.312x10^{-9}$	$S.s^n$
n_1	0.982	0.185	
n_2	0.852	0.347	
n_3	0.692	0.052	
W	$3.826x10^{-9}$	$3.528x10^{-9}$	$S.s^{1/2}$
Goodness of Fit	$285.6x10^{-6}$	-	

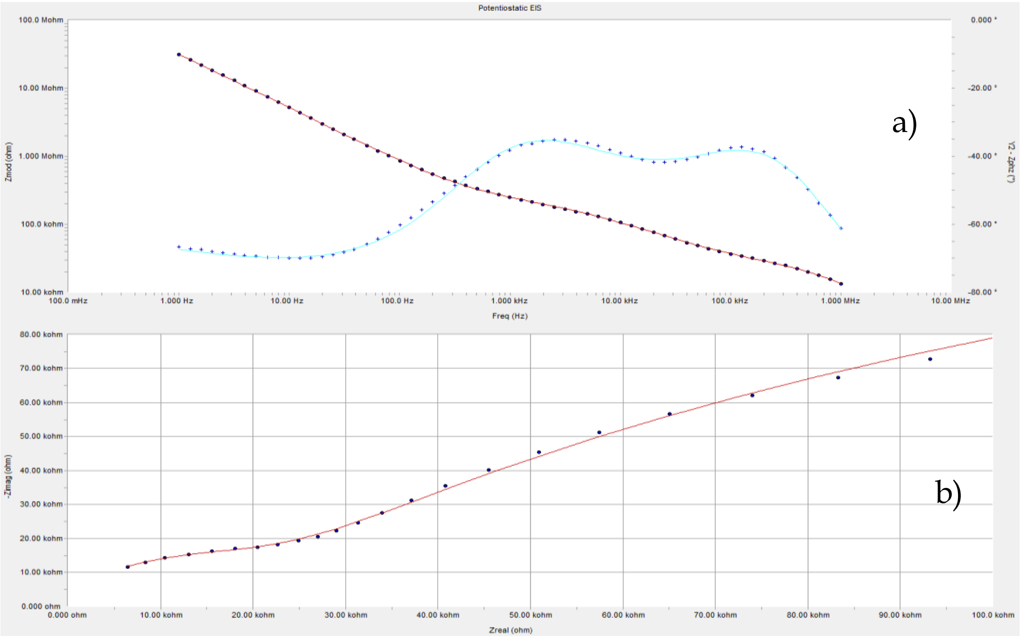

Figure 6.13 - Electrochemical Impedance Spectroscopy spectra given by Gamry Echem Analyst Software. Bode plot on (a) and niquist plot on (b) for a gold nanoflakes coating with the respective data fitting.

PEDOT/CNT

Table 6.15 - Equivalent circuit parameters calculated via Gamry Echem Analyst Software for fitting the data from an electrode modified with a solution of PEDOT and Carbon Nanotubes.

Parameter	Value	Error	Unit
R_E	2.171	2.269x10^3	Ω
R_P	22.23x10^3	5.36x10^3	Ω
R_{CT1}	461.7x10^3	7.88x10^3	Ω
R_{CT2}	30.14x10^6	143.9x10^9	Ω
CPE_1	39.18x10^{-12}	87.74x10^{-12}	S.s^n
CPE_2	519.3x10^{-12}	151.9x10^{-12}	S.s^n
CPE_3	38.34x10^{-9}	4.05x10^{-9}	S.s^n
n_1	0.921	0.156	
n_2	0.860	0.020	
n_3	0.982	0.021	
W	-2.334x10^{-19}	7.005x10^{-9}	S.s$^{1/2}$
Goodness of Fit	296.9x10^{-6}	-	

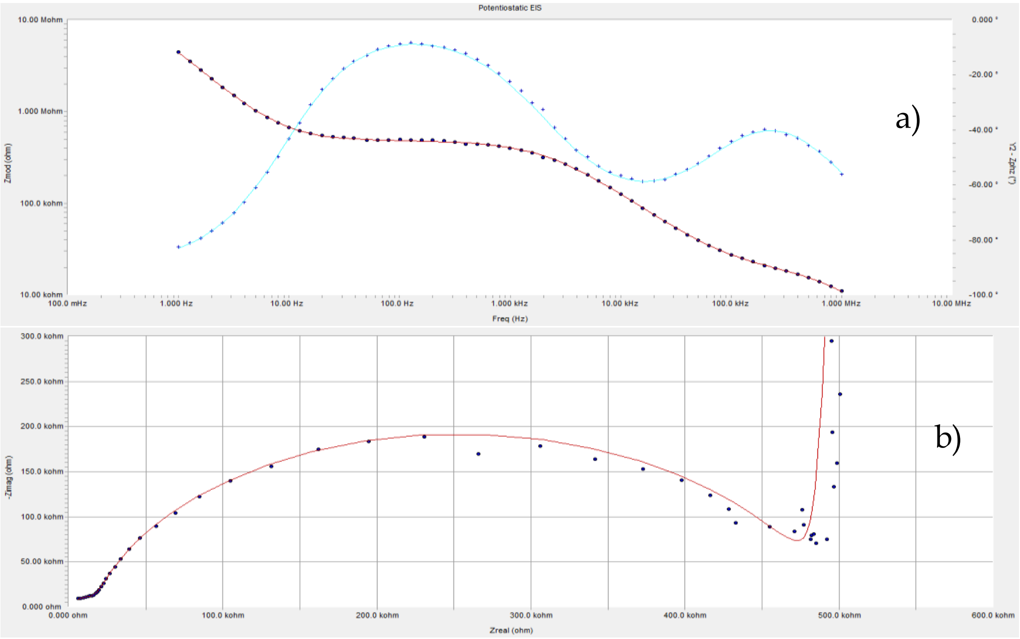

Figure 6.14 - Electrochemical Impedance Spectroscopy spectra given by Gamry Echem Analyst Software. Bode plot on (a) and nyquist plot on (b) for a PEDOT:CNT coating with the respective data fitting.

Section F

Acute neural data obtained for the different electrodes throughout the different recordings.

Table 6.16 – Acute neural experiment data from different recordings.

Modifications	**Spike # Max**	**Spike # Avg**	**Amplitude P2P Max**	**Amplitude P2P Avg**	**SNR Max**	**SNR Avg**	**Noise Level Min**	**Noise Level Avg**
Units	A.U	A.U	μV	μV	A.U	A.U	μV	μV
Recording #1								
Pristine	56	20±23	145.23	46.08±65.29	4.96	1.79±2.21	26.44	31.51±5.07
PEDOT	120	32±52	134.78	40.71±58.03	5.41	2.09±2.56	20.24	23.48±3.24
PEDOT:AuNPs	-	-	-	-	-	-	-	-
PEDOT:WO_3NPs	-	-	-	-	-	-	-	-
Au	-	-	-	-	-	-	-	-
Au:PVP	41	22±17	137.42	65.07±65.18	4.53	2.19±2.20	28.34	29.60±0.89
AuNPs	-	-	-	-	-	-	-	-
WO_3 NPs	-	-	-	-	-	-	-	-
Recording #2								
Pristine	1019	319±407	171.31	95.89±69.85	5.64	3.95±2.11	22.74	33.56±7.89
PEDOT	304	165±90	404.37	161.27±122.25	8.86	4.66±2.92	19.84	33.47±8.92
PEDOT:AuNPs	193	186±8	189.14	162.28±26.86	4.29	4.07±0.31	35.16	39.57±4.41
PEDOT:WO_3NPs	-	-	-	-	-	-	-	-
Au	139	73±50	148.29	95.14±57.15	5.52	3.85±2.59	22.10	24.65±2.79
Au:PVP	489	330±150	173.12	111.18±78.69	4.25	2.66±2.06	39.78	41.99±1.81
AuNPs	-	-	-	-	-	-	-	-
WO_3 NPs	-	-	-	-	-	-	-	-
Recording #3								
Pristine	121	47±42	216.98	122.98±70.92	6.05	3.95±1.93	20.18	32.04±8.79
PEDOT	145	66±45	294.07	143.77±103.94	7.96	4.01±2.49	27.96	34.75±4.01
PEDOT:AuNPs	337	200±137	184.98	151.9±46.78	4.6	4.03±0.58	34.4	37.31±2.91
PEDOT:WO_3NPs	-	-	-	-	-	-	-	-
Au	63	29±22	121.03	116.61±4.89	4.81	4.17±0.39	25.18	28.14±1.91
Au:PVP	338	236±71	176.55	137.21±68.23	4.97	3.50±1.62	28.82	39.83±5.95
AuNPs	56	56	129.87	43.29±74.98	4.95	2.48±2.48	26.22	26.22
WO_3 NPs	-	-	-	-	-	-	-	-

Section G

Table 6.17 – Electrodeposition parameters used for coatings with different materials.

		Time (s)							
I (nA)	**Material**	0.5	1	2	5	8	10	12.5	15
-5	Au:PVP	-	-	14%*** (D1)	-	-	-	-	-
	AuNPs	-	-	-	-	-	-	-	-
	WO_3NPs	-	-	13%*** (D1)	-	-	NCZ	-	-
-10	WO_3NPs	-	-	NCZ	-	-	NCZ	-	-
-15	WO_3NPs	-	-	NCZ	-	-	NCZ	-	-
-20	WO_3NPs	-	-	10%*** (D1)	-	-	7%*** (D1)	-	-
-30	Commercial Au	-	-	-	-	-	-	-	-
	Au:PVP	-	-	-	-	-	-	-	-
	AuNPs	-	-	-	-	-	-	-	-
	WO_3NPs	-	-	NCZ	-	28%** (D1)	56%** (D1)	-	22%*** (D1)
	AuNPs on PEDOT	-	-	-	-	-	-	-	-
	WO_3NPs on PEDOT	-	-	-	-	-	-	-	-
-60	AuNPs	-	-	-	-	-	-	-	-
	WO_3NPs	-	-	NCZ	-	-	NCZ	-	-
-120	Commercial Au	-	-	-	-	-	-	-	-
	AuNPs	-	-	-	-	-	-	-	-
	WO_3NPs	-	-	40%** (D2)	-	15%** (D1)	-	-	-
-240	WO_3NPs	-	46%** (D2)	-	-	-	-	-	-
-480	WO_3NPs	42%** (D2)	-	-	-	-	-	-	-
+5	WO_3NPs	-	-	-	EC	-	EC	-	-
+10	WO_3NPs	-	-	-	-	-	-	-	-
+15	WO_3NPs	-	-	-	-	-	-	-	-
+20	WO_3NPs	-	-	-	-	-	-	-	-
+30	AuNPs	-	-	-	-	-	-	-	-
	WO_3NPs	-	-	-	-	-	EC	-	-
	PEDOT	-	-	-	93%* (D4)	-	-	-	97%* (D3)
	PEDOT + AuNPs	-	-	-	NCZ	-	-	-	-
	PEDOT + CNTs	-	-	-	-	-	-	-	-

		Time (s)							
I (nA)	**Material**	17	20	25	30	40	50	60	90
-5	Au:PVP	-	-	-	40%** (D1)	-	-	-	-
	AuNPs	-	-	-	9%*** (D1)	-	-	-	-
	WO_3NPs	-	-	-	18%*** (D1)	-	-	10%*** (D1)	-
-10	WO_3NPs	-	-	-	13%*** (D1)	-	-	-	-
-15	WO_3NPs	-	-	-	-	-	-	-	-
-20	WO_3NPs	-	-	-	-	-	-	-	-
-30	Commercial Au	-	-	-	NCZ	15%*** (D1)	-	54%** (D1)	40%** (D1)
	Au:PVP	-	-	-	74%** (D2)	-	-	-	-
	AuNPs	-	-	-	NCZ	-	-	NCZ	-
	WO_3NPs	-	-	-	23%** (D2)	-	-	20%** (D2)	-
	AuNPs on PEDOT	-	-	-	-	-	-	-	-
	WO_3NPs on PEDOT	-	-	-	-	-	-	NCZ	-
-60	AuNPs	-	-	-	-	-	-	-	-
	WO_3NPs	-	-	-	-	-	-	-	-
-120	Commercial Au	-	-	-	-	-	-	-	-
	AuNPs	-	-	-	-	-	-	-	-
	WO_3NPs	-	-	-	-	15%** (D1)	-	-	-
-240	WO_3NPs	-	-	-	-	-	-	-	-
-480	WO_3NPs	-	-	-	-	-	-	-	-
+5	WO_3NPs	-	EC	-	EC	-	EC	-	EC
+10	WO_3NPs	-	-	EC	-	-	-	-	-
+15	WO_3NPs	EC	-	-	-	-	-	-	-
+20	WO_3NPs	-	-	-	-	-	-	-	-
+30	AuNPs	-	-	-	-	-	-	EC	-
	WO_3NPs	-	EC	-	-	-	-	EC	-
	PEDOT	-	-	-	97%* (D1)	-	-	-	-
	PEDOT + AuNPs	-	-	-	97%* (D2)	-	-	-	-
	PEDOT + CNTs	-	-	-	94%* (D2)	-	-	-	-

		Time (s)			
I (nA)	**Material**	120	180	300	600
-5	Au:PVP	52%** (D1)	-	-	-
	AuNPs	-	-	-	-
	WO_3NPs	-	12%*** (D1)	2%*** (D1)	-
-10	WO_3NPs	-	9%*** (D1)	-	-
-15	WO_3NPs	-	-	-	-
-20	WO_3NPs	-	-	-	-
-30	Commercial Au	78%** (D4)	95%** (D2)	-	-
	Au:PVP	82%** (D3)	58%** (D2)	-	-
	AuNPs	NCZ	NCZ	NCZ	NCZ
	WO_3NPs	50%** (D2)	36%** (D1)	-	-
	AuNPs on PEDOT	-	-	-	-
	WO_3NPs on PEDOT	-	-	-	-
-60	AuNPs	NCZ	-	-	-
	WO_3NPs	37%** (D2)	-	NCZ	-
-120	Commercial Au	85% *** (D3)	-	-	-
	AuNPs	NCZ	-	NCZ	-
	WO_3NPs	85%** (D2)	-	-	-
-240	WO_3NPs	-	-	-	-
-480	WO_3NPs	-	-	-	-
+5	WO_3NPs	-	-	-	-
+10	WO_3NPs	-	-	-	-
+15	WO_3NPs		-	-	-
+20	WO_3NPs	-	-	-	-
+30	AuNPs	EC	-	EC	-
	WO_3NPs	EC	EC	-	-
	PEDOT	98%* (D1)	-	-	-
	PEDOT + AuNPs	-	-	-	-
	PEDOT + CNTs	-	-	-	-

Table Legend:

* - Stable impedance, excellent deposition;

** - Unstable impedance (stabilizes at impedance values superior than those after deposition), good deposition;

*** - Very unstable impedance (normally returns to initial values), bad deposition;

D1 – One sample;

D2 – Between 2 and 5 samples;

D3 – Between 5 and 10 samples;

D4 – More than 10 samples;

EC – Electrochemical cleaning of the probe electrodes;

NCZ – No change in impedance observed, no deposition.

Section H

Atlas map corresponding to the section where the silicon HPD was inserted during surgical procedure.

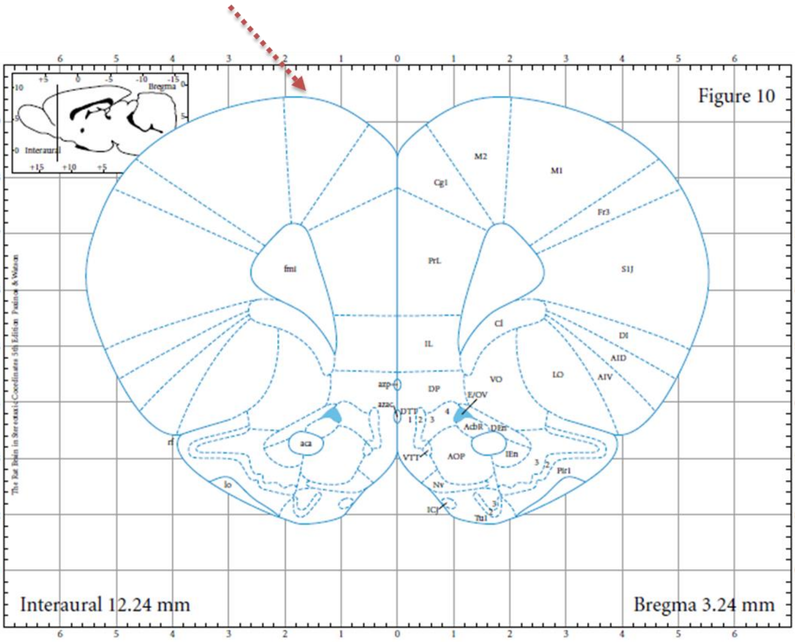

Figure 6.15 – Atlas map of the rodents' brain where the probe was inserted (red arrow pointing insertion region). Insertion coordinates are AP (Y) 3.24 mm, ML (X) 1.75 mm and (Z) -3.417 mm.

Table 6.18 – Coordinates for the different recordings, respectively.

	ML (left to right)	Z (top to bottom)
Rec #1	1.647 mm	-4.138 mm
Rec #2	1.692 mm	-4.188 mm
Rec #3	1.730 mm	-4.230 mm